**AWARD NUMBER:** W81XWH-18-1-0282

**TITLE:** Direct Imaging of Modulatory Neurotransmitters Using Synthetic Nanosensors to Understand and Treat Parkinson's Disease

**PRINCIPAL INVESTIGATOR:** Dr. Jackson T. Del Bonis-O'Donnell

**CONTRACTING ORGANIZATION:** The Regents of the University of California

**REPORT DATE:** AUGUST 2020

**TYPE OF REPORT:** Annual Report

**PREPARED FOR:** U.S. Army Medical Research and Materiel Command
Fort Detrick, Maryland 21702-5012

**DISTRIBUTION STATEMENT:** Approved for Public Release; Distribution Unlimited

# REPORT DOCUMENTATION PAGE

*Form Approved*
*OMB No. 0704-0188*

| | | |
|---|---|---|
| **1. REPORT DATE**<br>AUGUST 2020 | **2. REPORT TYPE**<br>Annual | **3. DATES COVERED**<br>7/15/19–7/14/2020 |

**4. TITLE AND SUBTITLE**
Direct Imaging of Modulatory Neurotransmitters Using Synthetic Nanosensors to Understand and Treat Parkinson's Disease

**5a. CONTRACT NUMBER**
W81XWH-18-1-0282

**5b. GRANT NUMBER**
W81XWH-18-1-0282

**5c. PROGRAM ELEMENT NUMBER**

**6. AUTHOR(S)**

Dr. Jackson Del Bonis-O'Donnell

E-Mail: jtdo@berkeley.edu

**5d. PROJECT NUMBER**

**5e. TASK NUMBER**

**5f. WORK UNIT NUMBER**

**7. PERFORMING ORGANIZATION NAME(S) AND ADDRESS(ES)**

Regents of the University of California
UNIVERSITY OF CALIFORNIA, BERKELEY 2150 SHATTUCK
AVE RM 313 BERKELEY CA 94704-5940

**8. PERFORMING ORGANIZATION REPORT NUMBER**

**9. SPONSORING / MONITORING AGENCY NAME(S) AND ADDRESS(ES)**

U.S. Army Medical Research and Development Command
Fort Detrick, Maryland 21702-5012

**10. SPONSOR/MONITOR'S ACRONYM(S)**

**11. SPONSOR/MONITOR'S REPORT NUMBER(S)**

**12. DISTRIBUTION / AVAILABILITY STATEMENT**

Approved for Public Release; Distribution Unlimited

**13. SUPPLEMENTARY NOTES**

**14. ABSTRACT**

Nanosensors for the optical detection of dopamine in brain slice has been validated in wildtype C57/C6 mice as well as a Parkinson's model mouse. Using nanosensors, endogenous dopamine release in striatal brain slice is triggered by electrical stimulation and quantified using microscopy. We have established the workflow for this procedure and have prepared a population of Parkinson's and wildtype mice to image in the coming quarter. We have confirmed that the method can quantitatively distinguish dopamine release between subregions of the striatum, a critical step in confirming the method for use in Parkinson's studies. COVID-19 shutdowns stalled research starting in Mar. Research facilities are reopening and the project is expected to resume this quarter.

**15. SUBJECT TERMS**

Parkinson's disease, dopamine, neuromodulation, imaging

| **16. SECURITY CLASSIFICATION OF:** | | | **17. LIMITATION OF ABSTRACT** | **18. NUMBER OF PAGES** | **19a. NAME OF RESPONSIBLE PERSON**<br>USAMRMC |
|---|---|---|---|---|---|
| **a. REPORT**<br>Unclassified | **b. ABSTRACT**<br>Unclassified | **c. THIS PAGE**<br>Unclassified | Unclassified | **41** | **19b. TELEPHONE NUMBER** *(include area code)* |

**Standard Form 298 (Rev. 8-98)**
**Prescribed by ANSI Std. Z39.18**

TABLE OF CONTENTS

## 1. INTRODUCTION:

Our work aims to enable the direct visualization of dopamine transmission in living brain tissue of a PD mouse model leveraging our expertise with a new class of infrared dopamine nanosensors. Detailed measurements of neurotransmission at the molecular level with high spatial and temporal resolution will provide unprecedented insight into the mechanism of dopaminergic aberrations in PD and their effects on neuroplasticity. Additionally, these methods will aid in understanding the interplay of the prescribed drug L-DOPA and changes to dopamine neurotransmission and dyskinesia side-effects.

## 2. KEYWORDS:

Fluorescence imaging – Nanomaterials – Sensing – Dopamine – Parkinson's Disease – Neuromodulators – Dyskinesia

## 3. ACCOMPLISHMENTS:

**What were the major goals of the project?**

**Major Task 1: Image nanosensors embedded within acute striatal mice brain slice and confirm dopamine sensing**

Subtask 1: Optimize nanosensor injection into extracellular space of acute brain slices. Monitor distribution using infrared fluorescence microscopy. *Completed as of Nov 2018.*

Subtask 2: Image nanosensor response to stimulated dopamine release using potassium and optogenetic stimulation. *Completed as of Nov 2018.*

Subtask 3: Monitor neuroinflammation resulting from nanosensor injections. *Ongoing.*

**Major Task 2: Quantify differences in dopamine release and reuptake from near-infrared imaging of acute slices from PD model mice**

Subtask 1: Preparation of LPS and alpha-synuclein (AS) lesioned mice. Pilot group of mice received LPS and sham injections. Imaging workflow for dopamine established. Issues with TH-immunohistochemical labeling of slices needs to be overcome with new protocol. *Months 10-30. 50% complete.*

Subtask 2: Near-infrared imaging of nanosensor injected slices of PD and control mice to compare dopamine release and uptake dynamics. Simultaneous GCaMP and/or FSCV measurements. *Ongoing. Months 10-30.*

Subtask 3: Analyze image data and quantify release dynamics and fit to dynamic and kinetic models. Compare to GCamp and FSCV. *Ongoing. Months 10-30.*

**Major Task 3: Image changes in neurotransmission between PD and WT mice resulting from L- DOPA treatment**

Subtask 1: Prepare L-DOPA treated mice of both PD and WT. *Months 15-30.*

Subtask 2: Perform near-infrared microscopy of acute striatal slices for PD and WT mice treated with L- DOPA. Repeat for control mice. *Months 15-30.*

Subtask 3: Analyze image data and quantify release dynamics and fit to dynamic and kinetic models. Determine impact of L-DOPA treatment on dopamine neurotransmission in PD and WT mice. *Months 15-30.*

**What was accomplished under these goals?**

1) Major Activities:

We finalized the formulation of our near-infrared dopamine nanosensors and established a workflow for their use to image dopamine from brain slices obtained from mice. The full details of the technique that will be utilized for the remainder of the project is outlined in our recent publication (see Appendix I). (Major Task 1)

We performed stereotaxic injections of lipopolysaccharide (LPS) into the substantia nigra pars compacta (SNc) of C57/B6J mice to induce a Parkinsonian phenotype as outlined in our statement of work and approved animal use protocol. Acute brain sections from the dorsal striatum were taken from these mice for imaging. Dopamine nanosensors were introduced into the tissue and electrical stimulation was used to induce the release of dopamine. Imaging the changes to the near-infrared fluorescence of the nanosensors provide us with a quantification of the amount of dopamine released by the tissue. Since the finalization of the slice preparation and stimulation protocols, we have collected and quantified images of dopamine release from striatal tissue from n=3 LPS injected mice and n=2 PBS (sham/control) injected mice. We collect images from both the lesioned and non-lesioned hemispheres of the dorsal striatum. (subtasks of Major Task 2)

Software was written to process video files, perform spatial analysis, and fit dopamine release and decay curves for the nanosensor data collected. All data from LPS and sham mice was analyzed, including imaging data from lesioned and non-lesioned hemispheres. (subtask of Major Task 1 & 2)

TH-staining was performed in the SNc of mice that received LPS injections. Stained slices were imaged under a fluorescent microscope to determine the number of dopaminergic neurons present in the SNc in the lesioned hemisphere compared to the non-lesioned hemisphere.

Inflammatory markers from SIM-A9 cells were quantified after exposure to the SWNT-based nanosensor to evaluate toxicity and potential complications arising from tissue inflammation. Additionally, electrophysiology measurements were performed to evaluate the impact on firing rate of neurons ex vivo and in the presence of nanosensor.

Nanosensor fluorescence data was collected from acute coronal slice of WT mice (n=5). The differences between density of release sites (speculated), peak evoked dopamine release, and reuptake constants was quantified and compared across the dorsal lateral striatum and nucleus accumbens core.

**Due to the COVID-19 shutdown, all research activities were halted in March. Labs are return to operation at an extremely limited capacity. This project is in the process of resuming and actions are being taken to continue work on Major Task 2.**

2) Specific objectives:

Our objective was to finalize the new procedure for quantifying dopamine release from brain slice using our nanosensor technology. The results are included in our recent publication (see Appendix I).

One of the major goals of the project is to confirm the expected decrease in dopamine release in the dorsal striatum of mice receiving an LPS injection in the SNc. Such a decrease in overall dopamine levels and release amounts has been shown in the literature using other techniques, such as fast scan cyclic voltammetry and HPLC/MS, albeit without spatial resolution. From this data, we hope to quantify changes to both the release site density, the amount of dopamine released per release site, and changes to reuptake kinetics.

One of our major tasks is to evaluate the biocompatibility of the nanosensors in neuronal tissue. We performed morphological analysis, RNAseq, and electrophysiology experiments to determine the impact that the nanosensors have on neuronal cells.

The ability of nanosensors to reliably quantify dopamine with an accuracy and systematic experimental variance sufficient to distinguish differences in dopamine release between striatal brain regions, between lesioned and non-lesioned hemispheres, and with a consistency that enables comparisons between animals had yet been rigorously evaluated. In the past year, we performed a series of control experiments to confirm that the sensors are accurate enough and our technique and procedures consistent enough to quantify biologically relevant differences in dopamine release and reuptake between different brain regions.

3) Results:

Major Task 1:

Detailed results validating our technique are provided in our publication (Appendix I).

Major Task 2:

Our results demonstrate no statistically significant difference in evoked dopamine release as measured using near-infrared fluorescent dopamine nanosensors and fluorescence microscopy (Major Task 2, Subtask 1 & 2). Results are outlined in **Figure 1**. This is contrary to what is expected for acute lipopolysaccharide (LPS) injection into substantia pars compacta (SNc). For the last 3 months, we worked to determine whether this discrepancy was due to either i) the LPS lesion not inducing dopaminergic cell death, or ii) the dopamine nanosensor not being capable of distinguishing changes in dopamine release. Another possibility is that peak evoked dopamine release is not impacted by LPS lesioning of the SNc even if overall levels decrease. We are reaching out to colleagues for more information on this topic. After this is resolved, we will repeat Subtask 1 & 2 of Major Task 2 and move on to Major task 3.

TH-staining of fixed brain tissue slices obtained 2 weeks after LPS-lesioning show no decrease in the number of cell bodies in the SNc compared to the non-lesioned hemisphere (**Figure 2a**). This suggests that the injections are not inducing a Parkinsonian phenotype, i.e. a loss of dopaminergic neurons and the associated decrease in striatal dopamine. Moving forward, we are trying higher concentrations of LPS (10 ug/uL) as well as obtaining LPS from a different source (Salmonella minnesota, Sigma Aldrich).

To confirm that the dopamine nanosensors are capable of quantifying differences in dopamine release, we sought to map out the differences in evoked dopamine release in a single slice. A dorsal to ventral decrease in peak evoked dopamine release has been previously reported in literature. We confirmed that our nanosensor platform can optically quantify this gradient across the striatum **(Figure 3)** from n=3 mice. These results give us confidence that the platform is robust enough to provide insight into biologically relevant variation in dopamine release dynamics, specifically those induced by Parkinson's disease models as part of our Major Task 1 &2.

Furthermore, we began leveraging the unique imaging data obtained using our technique to investigate the spatial dependencies of dopamine release at a micron scale. This is unique in that no other technique to date has been able to leverage and quantify this type of information. **Figure 4** shows results analyzing population statistics of 20µM square ROIs shows which shows clear distinctions between DLS and NAc as well as subpopulations distinguished by their peak release and decay times. The ability to quantify these distinctions at such a fine spatial resolution will allow for new ways to investigate and probe the molecular underpinnings that drive circuits regulated by dopamine. Such analysis is particularly pertinent to understanding the details of dysregulation in Parkinson's disease.

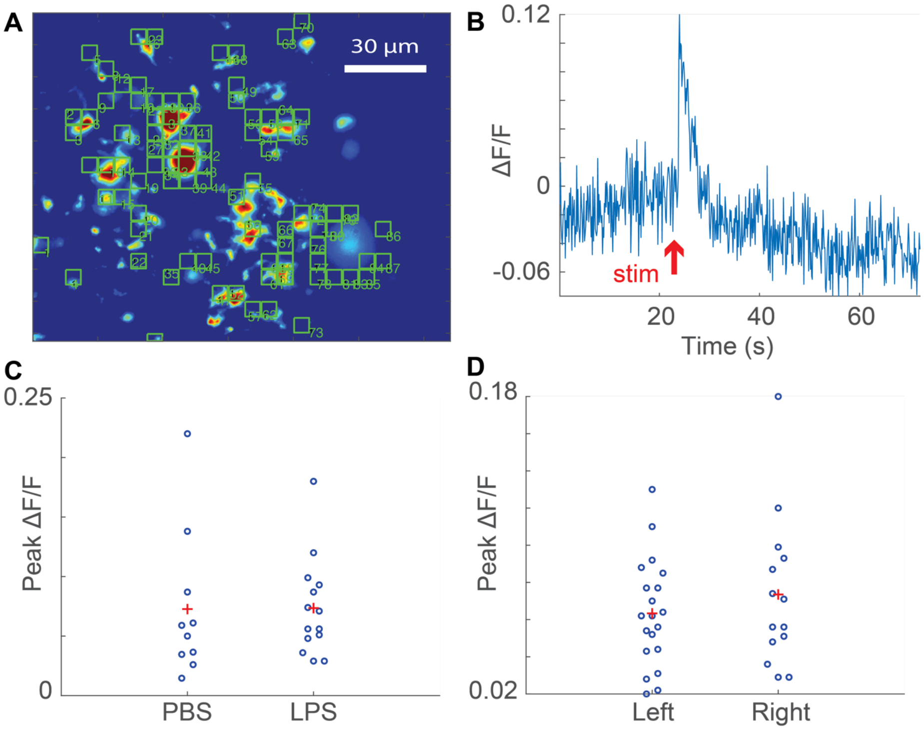

**Figure 1** (**A**) Representative mean projection image generated from a video recording of acute brain slice of dorsal striatum from mouse. Fluorescence signal is generated by our near-infrared nanosensors infused in the tissue. Images are obtained using an InGaAs short wavelength near-infrared camera. Our algorithm identifies regions of interest (green squares) in each video where a statistically significant increase in fluorescence intensity occurs following electrical stimulation. (**B**) Representative trace of change in fluorescence intensity (dF/F) of a region of interest over time. A red arrow indicates the time of electrical stimulation. The increase in dF/F following this time point indicates that dopaminergic neurons are releasing dopamine into the extracellular space and binding to our nanosensors. (**C**) Preliminary data collecting peak dF/F signal after stimulation for n=2 PBS injected mice and n=3 LPS injected mice.

Images were collected from the right (injected) hemisphere. (**D**) Preliminary data collecting peak dF/F signal after stimulation and comparing the left (non-lesioned) hemisphere to the right (lesioned) hemisphere for n=3 LPS injected mice.

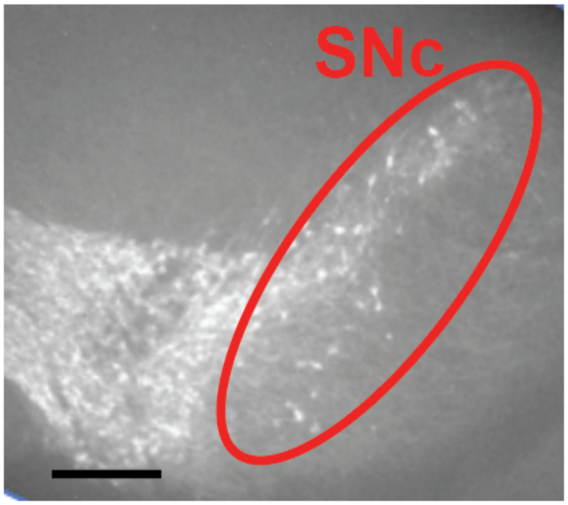

**Figure 2** Immunohistochemical labeling of a brain slice obtained from an LPS-lesioned mouse using a tyrosine-hydroxylase antibody. No loss of dopaminergic neurons was observed.

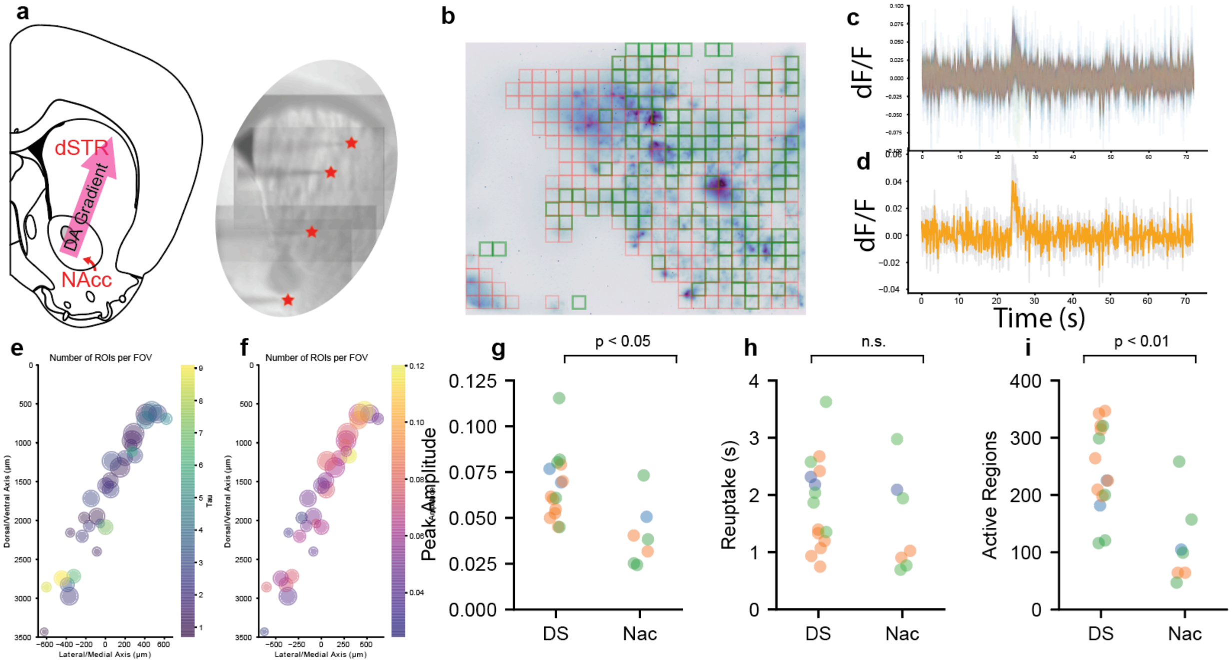

**Figure 3.** (a) Schematic depicting where electrically evoked dopamine was measured. We expect peak DA repease to be greater in DLS than in NAc. (b) Schematic depicting algorithmic processing of video data where active and inactive zones of dopamine release are identified and marked for further analysis. (c) dF/F signal from nanosensors plotted from each active ROI in a single field of view (top) and average trace with bounds depicting standard deviation. Stimulation occurs at the 24 s mark. (e,f) Plots depicting spatial difference in number of active ROIs (circle diameter) and color depicting decay constant of transient (e) and peak amplitude (f). Plots of peak amplitude (g), decay constant (h), and number of active regions (i) averaged over FOV for different regions and n=3 mice.

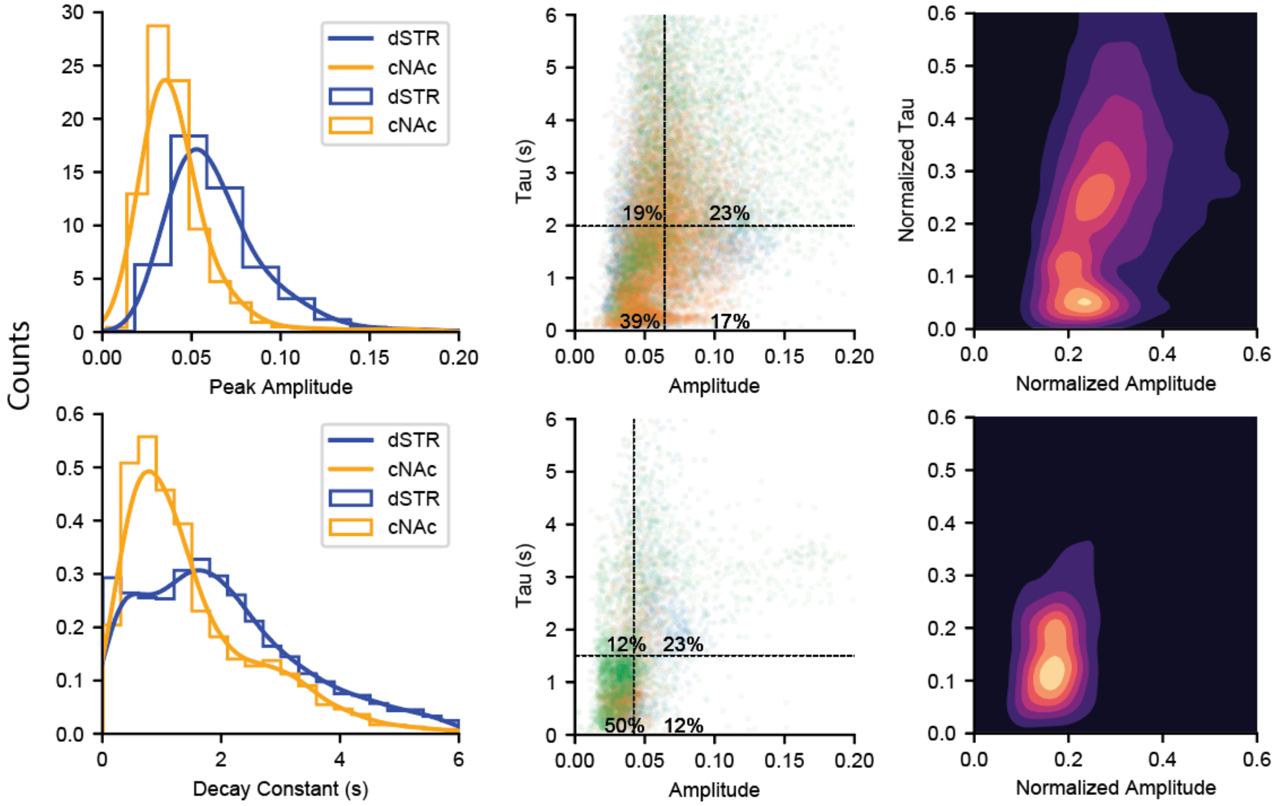

**Figure 4.** (left) Data pooled from nanosensor fluorescence data on an ROI by ROI basis from n=3 mice. Data is fit using a kernel density estimator to show distinct population differences between 20 µm square regions of the DLS (top) and NAc (bottom). (center) Differences in regional subpopulations of dopamine dynamics based on their peak dopamine release volume and decay constant (analogous to reuptake). Clear distinctions are shown between dorsal striatum (top) and nucleus accumbens (bottom). (right) Same as center plots, but contours fit using a kernel density enstimator. These results highlight that spatial hetereogeneity in dopamine release and modulation between different sub-nuclei of the striatum exist at the 10s of micron scale.

### What opportunities for training and professional development has the project provided?

*If the project was not intended to provide training and professional development opportunities or there is nothing significant to report during this reporting period, state "Nothing to Report."*

The PI, Dr. Jackson Del Bonis-O'Donnell, has been trained in basic mouse husbandry and breeding, anesthesia, perfusion, preparation of brain slices for imaging and electrophysiology, as well as performing sterile survival stereotaxic injection surgeries of agents into the brain of mice. These are skills essential to the current project and allow for data to be collected at a faster pace because both he and a collaborator can prepare mice for the project. These are also essential skills for future projects as he transitions into an independent research career involving topics in quantitative neurobiology.
Additionally, the project provided research experience for a undergraduate/lab tech who has now successfully transitioned into a graduate research program elsewhere.

### How were the results disseminated to communities of interest?

The PI, Dr. Jackson Del Bonis-O'Donnell, has attended several conferences in which the methodologies utilized in this project, i.e. using nanosensors to image dopamine release from neurons, were shared. These included talks given at the Annual Meeting of the American Institute of Chemical Engineers in November 2018. This meeting has thousands of attendees and provides an excellent opportunity to share our research with many undergraduate students, graduate students and early-career industry and government employees. Dr. Del Bonis-O'Donnell also gave a talk at a DARPA meeting related to brain machine interfaces in April 2019. This provided a unique opportunity to interface with many different labs and government teams interested in ways that new techniques can provide quantitative feedback to use for interfacing with the brain. Additionally, Dr. Del Bonis-O'Donnell presented aspects of this work at the American Chemical Society Fall meeting 2019.

Dr. Del Bonis-O'Donnell has published analysis code in MATLAB in an app available to the public at www.github.com/jtdbod/

**What do you plan to do during the next reporting period to accomplish the goals?**

Due to the COVID-19 closures, experiments will resume Sept 2020 now that infrastructure is available on a limited basis. We will resume LPS injections and re-perform measurements outlined in Major Task 2. We will confirm, via tyrosine hydroxylase immunohistochemistry staining that the LPS is lesioning dopaminergic neurons in the SNc as expected.

A manuscript outlining results of our new spatial analysis of dopamine in DLS and NAc as well as the micron scale ROI population analysis of dopamine release is in preparation and will likely be submitted by next reporting period.

## 4. IMPACT:

**What was the impact on the development of the principal discipline(s) of the project?**

Many neurodegenerative diseases and psychiatric disorders are related to changes in how neurons release chemicals known as neuromodulators. Most drug therapies attempt to manipulate the levels of neuromodulators in your brain to correct for any imbalances. However, there exist few, if any, ways in which to accurately measure how these drugs impact how much neuromodulator a neuron releases as well as how these levels change in real time. Using our engineered nanosensors, we can visualize the release of the neuromodulator dopamine and easily see how the amount of dopamine release changes as a result of a disease, disorder, or therapy, potentially at the single neuron level. For Parkinson's disease, this means we can explore the details underlying changes to dopamine release and how it impacts brain function. Additionally, we can use this technique to better understand why the most common Parkinson's therapy, levodopa, produces is negative side-effects, and potentially inform new ways to reduce these effects and improve therapies.

**What was the impact on other disciplines?**

The ability to image and quantify catecholamines, such as dopamine, in real-time with high spatial resolution will be a powerful tool for the study of the neurobiology of disease as well as inform fundamental understanding of brain function at a chemical level. The more quantitatively we understand these systems, the better the pharmaceutical industry can develop and test new therapies aimed towards difficult to treat patients ranging from neurodegenerative diseases to psychiatric disorders.

**What was the impact on technology transfer?**

The methods we use for this project are included in a recent patent filing by Landry, Markita Del Carpio P. (Berkeley, CA, US), Wilbrecht, Linda A. (Berkeley, CA, US), Del Bonis-O'Donnell, Jackson Travis (Berkeley, CA, US), Beyene, Abraham G. (Berkeley, CA, US). Application number: 16/373542, Filing date: 04/02/2019.

**What was the impact on society beyond science and technology?**

It is the hope of the principal investigator that the methods and results of this project will help to better inform the development of drug therapies for patients suffering from neurodegenerative disease and psychiatric disorders. An improved understanding of the molecular and chemical mechanisms of brain function could ultimately improve the quality of life for millions of Americans, promote new growth in the pharmaceutical sectors, and influence policy choices related to these illnesses for public health.

## 5. CHANGES/PROBLEMS:

**Changes in approach and reasons for change**

Nothing to report.

**Actual or anticipated problems or delays and actions or plans to resolve them**

Due to COVID-19, our research facilities are only operational in a very limited capacity. As such, availability of equipment for performing the necessary surgeries and measurements will be limited. Currently, Dr. Jackson Del Bonis-O’Donnell has limited laboratory time and is the sole contributor to the project. As such, we anticipate output to be ~25% of what can typically be expected given the current restrictions.

**Changes that had a significant impact on expenditures**

Animal experiments were delayed because of a staff change on the part of the collaborator performing the stereotaxic injections outlined in the approved AUP. During that time, Dr. Del Bonis-O’Donnell went through training and certification and is now approved and routinely performing stereotaxic injections for the project. This delay postponed much of the animal and surgical costs. Additionally, expenditures for electrodes has been delayed because we have been using custom demo electrodes while we determine the optimal fabrication. Once finalized, we will be purchasing enough for the remainder of the experiments in the project.

COVID-19 has impacted our ability to purchase from the grant. However, the re-budgeting has allowed for the PI to continue the project through an NCE and the remaining funds are now allocated for the remaining animal and care costs. All other remaining supplies necessary for the project are already purchased and available.

**Significant changes in use or care of human subjects, vertebrate animals, biohazards, and/or select agents**
Nothing to report.

**Significant changes in use or care of human subjects**
Nothing to report.

**Significant changes in use or care of vertebrate animals**
Nothing to report.

**Significant changes in use of biohazards and/or select agents**
Nothing to report.

## 6. PRODUCTS:

- **Publications, conference papers, and presentations**

  **Journal publications.**
  Beyene, A.G., Delevich, K., Del Bonis-O'Donnell, J.T., Piekarski, D.J., Lin, W.C., Thomas, A.W., Yang, S.J., Kosillo, P., Yang, D., Prounis, G.S. and Wilbrecht, L., 2019. Imaging striatal dopamine release using a nongenetically encoded near infrared fluorescent catecholamine nanosensor. Science advances, 5(7), p.eaaw3108. Acknowledgment of federal support: no, PI was not yet funded by grant for the data collected in this manuscript.

  **Books or other non-periodical, one-time publications.**
  Nothing to report.

  **Other publications, conference papers and presentations**.
  Presentations:
  American Institute of Chemical Engineers Annual Meeting. November 2018.
  DARPA Brain Machine Interfaces Workgroup Meeting. April 2019.
  American Chemical Society Fall Meeting. August 2019.

- **Website(s) or other Internet site(s)**

  https://github.com/jtdbod/Nanosensor-Brain-Imaging - website hosting video analysis code.
  https://github.com/jtdbod/Nanosensor-Imaging-App - website hosting new code

  landrylab.com – group website highlighting results, publications and research focus.

- **Technologies or techniques**
  The techniques used are outlined in the above publication and subsequent patent.

- **Inventions, patent applications, and/or licenses**

Title: Imaging Neurotransmitters In Vivo Using Functionalized Carbon Nanotubes
United States Patent Application 20190224342
Kind Code: A1
Application number: 16/373542
Filing Date: 04/02/2019

The contents of the above patent is related to the techniques used and optimized for the currently funded project.

- **Other Products**
  Nothing to report.

## 7. PARTICIPANTS & OTHER COLLABORATING ORGANIZATIONS

**What individuals have worked on the project?**

Name: Jackson Del Bonis-O'Donnell
Project Role: PI/Postdoc
Project Researcher Identifier: orcid.org/0000-0002-9135-2102
Nearest person month worked: 12
Contribution to Project: Prepared and imaged ex vivo brain slices obtained from LPS and sham injected mice. Further improved upon image processing and data analysis software. Analyzed imaging data obtained from imaging experiments. Optimized electrical stimulation protocol to increase robustness and repeatability of dopamine release and quantification. Constructing second imaging system to increase experimental throughput. Received training in stereotaxic surgery and performed LPS and PBS injections in SNc.

Name: Rhea Misra
Project Role: Collaborator/Research Associate
Research Identifier: N/A
Nearest Person Month Worked: N/A
Contribution to Project: Rhea is a research assistant in the Saijo laboratory (co-PI and mentor to Jackson Del Bonis-O'Donnell) that aided the PI (J. Del Bonis-O'Donnell) in performing stereotaxic injections of LPS and immunohistochemistry staining.
Funding Source: NIH (K. Saijo)

**Has there been a change in the active other support of the PD/PI(s) or senior/key personnel since the last reporting period?**

Dr. Jackson DelBonis-O'Donnell is now primarily advised by Prof. Dr. Linda Wilbrecht of the Helen Wills Neuroscience Institute at UC Berkeley. He continues this project through collaboration with Prof. Saijo and Prof. Landry.

**What other organizations were involved as partners?**

Nothing to report.

## 8. SPECIAL REPORTING REQUIREMENTS

**COLLABORATIVE AWARDS:**

**QUAD CHARTS:** See Appendix III

9. **APPENDICES:**
    - **I.** Published manuscripts related to techniques partially developed for this project.
    - **II.** Patent Application
    - **III.** Quad chart

## Appendix I

NEUROSCIENCE

# Imaging striatal dopamine release using a nongenetically encoded near infrared fluorescent catecholamine nanosensor

**Abraham G. Beyene[1], Kristen Delevich[2,3], Jackson Travis Del Bonis-O'Donnell[1], David J. Piekarski[1], Wan Chen Lin[2], A. Wren Thomas[3], Sarah J. Yang[1], Polina Kosillo[4], Darwin Yang[1], George S. Prounis[3], Linda Wilbrecht[2,3]*, Markita P. Landry[1,3,5,6]***

**Neuromodulation plays a critical role in brain function in both health and disease, and new tools that capture neuromodulation with high spatial and temporal resolution are needed. Here, we introduce a synthetic catecholamine nanosensor with fluorescent emission in the near infrared range (1000–1300 nm), near infrared catecholamine nanosensor (nIRCat). We demonstrate that nIRCats can be used to measure electrically and optogenetically evoked dopamine release in brain tissue, revealing hotspots with a median size of 2 μm. We also demonstrated that nIRCats are compatible with dopamine pharmacology and show D2 autoreceptor modulation of evoked dopamine release, which varied as a function of initial release magnitude at different hotspots. Together, our data demonstrate that nIRCats and other nanosensors of this class can serve as versatile synthetic optical tools to monitor neuromodulatory neurotransmitter release with high spatial resolution.**

## INTRODUCTION

The catecholamines dopamine (DA) and norepinephrine (NE) are neuromodulators known to play an important role in learning and attention and are implicated in multiple brain disorders (*1*–*5*). DA, in particular, is thought to play a critical role in learning (*6*), motivation (*7*, *8*), and motor control (*9*), and aberrations in DA neurotransmission are implicated in a wide range of neurological and psychiatric disorders including Parkinson's disease (*10*), schizophrenia (*11*), and addiction (*12*).

Modulatory neurotransmission is thought to occur on a broader spatial scale than classic neurotransmission, the latter of which is largely mediated by synaptic release of the amino acids glutamate (GLU) and γ-aminobutyric acid (GABA) in the central nervous system. In synaptic glutamatergic and GABAergic neurotransmission, neurotransmitter concentrations briefly rise in the synaptic cleft to mediate local communication between the pre- and postsynaptic neurons through the rapid activation of ligand-gated ion channels (*13*). In contrast, neuromodulators (catecholamines and neuropeptides) may diffuse beyond the synaptic cleft and act via extrasynaptically expressed metabotropic receptors (*14*–*19*). Thus, modulatory neurotransmitter activity extends beyond single synaptic partners and enables small numbers of neurons to modulate the activity of broader networks (*20*). The absence of direct change in ionic flux across cell membranes, which is measurable using available tools such as electrophysiology or genetically encoded voltage indicators, has necessitated the use of methods borrowed from analytical chemistry such as microdialysis and amperometry to study the dynamics of neuromodulation. However, the spatial limitations of fast-scan cyclic voltammetry (FSCV) and spatial and temporal limitations of microdialysis narrow our ability to interpret how neuromodulators affect the plasticity or function of individual neurons and synapses.

To understand how neuromodulation sculpts brain activity, we sought to develop new tools that can optically report modulatory neurotransmitter concentrations in the brain extracellular space (ECS) in a manner that is compatible with pharmacology and other available tools to image neural structure and activity. To this end, we designed a synthetic optical probe that can report extracellular catecholamine dynamics with high spatial and temporal fidelity within a unique near infrared (nIR) spectral profile. nIR fluorescent, polymer-functionalized semiconducting single-wall carbon nanotubes (SWNTs) provide a versatile platform for optical probe synthesis to image a diverse set of biomolecular analytes, several of which have shown in vivo functionality (*21*–*23*). In this work, we describe the design, characterization, and implementation of a nanoscale nIR nongenetically encoded fluorescent reporter that allows precise measurement of catecholamine dynamics in brain tissue. This technology makes use of an SWNT noncovalently functionalized with single-strand $(GT)_6$ oligonucleotides to form the nIR catecholamine nanosensor (nIRCat). nIRCats respond to DA with $\Delta F/F$ of up to 24-fold in the fluorescence emission window of 1000 to 1300 nm (*24*), a wavelength range that has shown utility for noninvasive through-skull imaging in mice (*25*).

First, we show in vitro characterization of the nanosensor's specificity for the catecholamines DA and NE and demonstrate its relative insensitivity to the neurotransmitters GABA, GLU, and acetylcholine (ACH), as well as the neuromodulators histamine, serotonin, tyramine, and octopamine. Second, we demonstrate that nIRCats exhibit a fractional change in fluorescence that has the dynamic range and signal-to-noise ratio to report DA efflux in response to brief electrical or optogenetic stimulation of dopaminergic terminals. Next, we use optogenetic stimulation to demonstrate selectivity of the nIRCat nanosensor response to dopaminergic over glutamatergic terminal stimulation. In both stimulation contexts, we show that bath application of D2-type DA receptor antagonist sulpiride and agonist

---

[1]Department of Chemical and Biomolecular Engineering, University of California, Berkeley, Berkeley, CA, USA. [2]Department of Psychology, University of California, Berkeley, Berkeley, CA, USA. [3]Helen Wills Neuroscience Institute, University of California, Berkeley, Berkeley, CA, USA. [4]Department of Molecular and Cell Biology, University of California, Berkeley, Berkeley, CA, USA. [5]California Institute for Quantitative Biosciences (QB3), Berkeley, CA, USA. [6]Chan Zuckerberg Biohub, San Francisco, CA, USA.

*Corresponding author. Email: landry@berkeley.edu (M.P.L.); wilbrecht@berkeley.edu (L.W.)

quinpirole modulates nIRCat signals in a manner consistent with predicted effects of presynaptic D2 autoreceptor manipulation. These latter experiments can resolve previously undetectable heterogeneity in D2 autoreceptor modulation of presynaptic DA release upon exposure to sulpiride or quinpirole. Last, we show that the presence of a DA reuptake inhibitor yields a prolonged nIRCat fluorescent signal, indicating that the sensors report a change in the time course of DA diffusion and reuptake in striatal brain tissue. These data indicate that nIRCats provide a unique synthetic tool compatible with pharmacology to interrogate the release, diffusion, and reuptake of neuromodulators in neural tissue.

## RESULTS

### A nIR DA and NE nanosensor

We report nIR fluorescent probes that enable imaging of synaptic and extrasynaptic catecholamines and their release and reuptake dynamics in the ECS of brain tissue. Using a previously established nanosensor generation platform (*26*, *27*), synthetic biomimetic polymers were pinned onto the surface of intrinsically nIR fluorescent SWNTs. The resulting noncovalent nanometer-scale conjugate produced the catecholamine-selective nIRCat (Fig. 1A). In in vitro solution phase experiments (see Materials and Methods), nIRCats exhibited a chirality-dependent maximal change in fluorescence ($\Delta F/F$) of up to 24 (Fig. 1, B and C) with a dynamic range of four orders of magnitude, reporting detectable fluorescence changes from 10 nM to 100 μM DA concentration (fig. S1A). nIRCats were also sensitive to NE with a maximal response of $\Delta F/F = 35$ and a similar dynamic range. We further found that nIRCats had an ~3-fold higher affinity for DA over NE (fig. S1A). nIRCats were insensitive to GABA, GLU, and ACH (Fig. 1C) and could report fluctuations in DA concentration in the presence of ascorbic acid, which is present in cerebrospinal fluid (fig. S1B). nIRCats were also insensitive to octopamine and tyramine, biogenic amines that act as neurotransmitters within invertebrates (Fig. 1C and fig. S1, C and D) and differ from DA by a single hydroxyl group in the case of tyramine or by the placement of a single hydroxyl group in the case of octopamine (fig. S1, C and D). Single-molecule imaging revealed that nIRCat signal in response to repeated perfusions of 10 μM DA was reversible, an important feature for measuring neuromodulator transients (fig. S2). In previous work, we performed stochastic simulations that suggest that nIRCats have sufficient sensitivity to detect physiologically relevant fluctuations in DA concentration in brain tissue arising from the activity of a single dopaminergic terminal, which can briefly exceed concentrations of 1 μM from the release site in a distance-dependent manner (*28*).

### Imaging of electrical stimulation–evoked DA release in striatal brain tissue

To determine the efficacy of nIRCats for imaging DA in brain tissue, we used brain slices from the dorsal striatum of the mouse. Given that the dorsal striatum is densely innervated by dopaminergic projections from the substantia nigra pars compacta (SNc) but lacks innervation from neurons that release NE (*29*), we leveraged nIRCats capacity to serve as a DA sensor in the striatum. Most of the neurons within the striatum are GABAergic medium spiny neurons (MSNs) with a minority fraction of interneuron populations that include GABAergic and cholinergic interneurons (*30*). Glutamatergic inputs from the cortex and thalamus are the major drivers of MSN activity, and dopaminergic terminals in close proximity to these inputs are thought to play an important role in modulating the activity of MSNs and plasticity at striatal synapses (*31*). Because of the composition of local axons, intrastriatal electrical stimulation is predicted to drive the release of a mix of neurotransmitter, including GABA, GLU, ACH, and DA, but negligible amounts of other catecholamines such as NE.

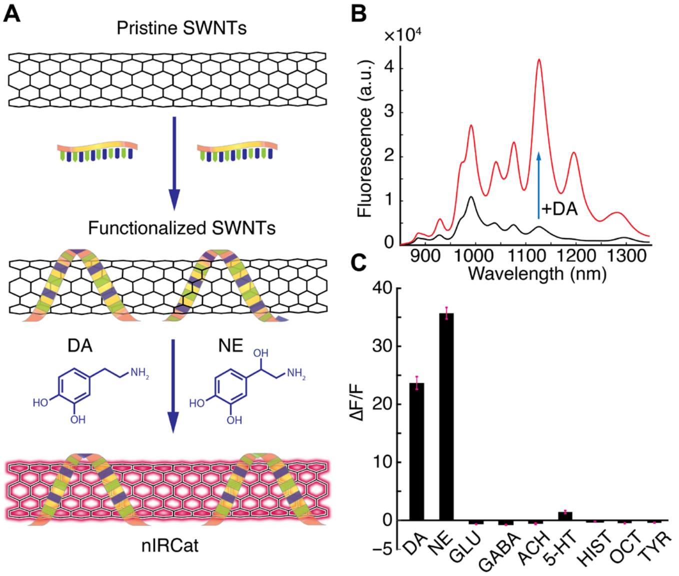

**Fig. 1. Synthesis and testing of nIRCats.** (**A**) Schematic of optical catecholamine reporters, nIRCats. Pristine SWNTs are functionalized with $(GT)_6$ oligonucleotides to generate turn-on optical reporters for DA and NE. (**B**) Fluorescence spectra of nIRCats before (black) and after (red) the addition of 10 μM of DA in an in vitro preparation in phosphate-buffered saline (PBS; without tissue). Multiple emission peaks correspond to unique SWNT chiralities contained within the multichirality mixture. a.u., arbitrary units. (**C**) Nanosensor optical response to 100 μM DA, NE, GLU, GABA, ACH, serotonin (5-HT), histamine (HIST), octopamine (OCT), and tyramine (TYR) (data from in vitro testing). Black bars represent averages from $n = 3$ independent measurements, and error bars are calculated as SDs of the $n = 3$ measurements.

Coronal mouse brain slices were prepared as described previously (*32*). Slices were subsequently incubated with artificial cerebrospinal fluid (ACSF) containing nIRCats (2 mg/liter) for 15 min to enable sensors to diffuse into the brain tissue (fig. S3A). Slices were subsequently rinsed to remove excess nIRCats and incubated in standard ACSF for another 15 min before imaging. Imaging of nIRCat fluorescence modulation in dorsal striatum was accomplished with a custom-built visible and nIR microscope to enable serial imaging of both visible (400 to 750 nm) and nIR (750 nm to 1700 nm) wavelengths on the same detector (fig. S3B). The nIRCat loading protocol enabled even and widespread labeling of the coronal slices containing the dorsal striatum (fig. S3C). Using this method, Godin *et al.* (*33*) have found that SWNTs localize in ECS. For the imaging procedure, a 785-nm laser for excitation of nIRCats or mercury bulb for generating bright-field images was directed onto the back focal plane of an epifluorescence upright microscope, and imaging channels were selected using a sliding mirror. Serially, either bright-field or nIR images were collected on a Ninox VIS-SWIR 640 broadband camera (Raptor Photonics) with appropriate dichroic filters (see Materials and Methods) and a 60× water-dipping objective (Nikon) providing an imaging field of 178 μm by 142 μm, likely containing hundreds of dopaminergic terminals.

To investigate striatal neuromodulator release with temporal control of tissue stimulation, we used a bipolar stimulating electrode to evoke terminal release within the dorsomedial striatum of the mouse (stimulus protocol: 3-ms-wide single square pulses over five biological replicates). We found that a single pulse could elicit a nIRCat signal transient (Fig. 2A and movie S1) and that increasing the strength of the stimulus led to larger evoked changes in nIRCat $\Delta F/F$ signal, $(\Delta F/F)_{\max}$ [0.1 mA = 0.047 ± 0.025, 0.3 mA = 0.122 ± 0.026, and 0.5 mA = 0.2 ± 0.033 (means ± SD); $n = 5$ for all measurements; $P = 0.008$ between 0.1 mA versus 0.3 mA and $P = 0.008$ between 0.3 mA versus 0.5 mA; Fig. 2B]. Similar responses were additionally obtained in an ex vivo slice of a previously wild-caught species of mouse (*Mus spicilegus*) (fig. S4, A and B). We included *M. spicilegus* to illustrate the potential for nIRCat use in species not typically found in laboratories and in which surgical or genetic manipulation may be a barrier to measurement.

To further test whether evoked nIRCat signals in the mouse tracked striatal DA release and reuptake kinetics, we investigated the effect of nomifensine, a DA reuptake inhibitor that slows the clearance of DA from the ECS by competitively binding to DA transporters (DATs). The addition of 10 μM nomifensine to the bath yielded nIRCat signal with higher peak fluorescence modulation [$(\Delta F/F)_{\max} = 0.108 \pm 0.029$ versus 0.189 ± 0.023 (means ± SD); $n = 3$; $P = 0.0178$] and a prolonged fluorescent signal compared to signals obtained in ACSF from the same field of view [decay time constant, $\tau = 2.43 \pm 0.24$ s versus 10.95 ± 1.15 s (means ± SD); $n = 3$; $P = 0.0002$; Fig. 2, A (top versus bottom) and C]. Application of 0 mM extracellular $Ca^{2+}$ ACSF abolished detectable nIRCat responses ($P < 0.0001$ relative to 2.5 mM $Ca^{2+}$ ACSF), whereas 4 mM $Ca^{2+}$ significantly enhanced evoked $\Delta F/F$ transients ($P < 0.0001$; Fig. 2D), confirming that nIRCat signals reflect a calcium-dependent process.

To identify nIRCat fluorescence change hotspots (i.e., regions of high $\Delta F/F$), we analyzed our video-rate acquisitions using a custom-built program that accounted for background fluorescence and identified regions with fluctuations in fluorescence intensity in the post-stimulation epoch (see Materials and Methods). We defined nIRCat $\Delta F/F$ hotspots as regions of interest (ROIs) based on a per-pixel stack projection of maximal $\Delta F/F$ in the imaging time series. Using data from single-pulse electrical stimulation experiments, we used custom software that identified ROIs whose sizes varied from 1 to 15 μm, with a log-normal distribution and a median ROI size of 2 μm (Fig. 2, E and F). Repeat stimulations with the same stimulation amplitude in fields of view of the dorsomedial striatum across biological replicates generated similar size distributions (fig. S5A). We found that $\Delta F/F$ hotspots do not necessarily correspond to high nIRCat labeling of the brain tissue, suggesting that the hotspots are a consequence of variation in DA release and not nanosensor loading in the tissue (fig. S5, B to F). Closer examination of several larger ROIs (>5 μm) suggested that these may be composed of smaller hotspots in close proximity (Fig. 2G and fig. S5, B and C).

For further examination of the temporal resolution of nIRCats, we compared the temporal profile of evoked transients measured with nIRCats to transients measured with FSCV. FSCV is a technique that has been widely used to measure temporal catecholamine dynamics both in vivo and in vitro in the striatum and other brain areas (*34*–*36*). FSCV and nIRCat experiments were conducted on separate experimental rigs with the same solutions, temperature settings, electrodes, and stimulation parameters. Evoked transients measured with FSCV (fig. S5G) and nIRCat fluorescence emission showed comparable temporal profiles in the rising phase [latency to peak: FSCV = 0.25 ± 0.0 s versus nIRCat = 0.40 ± 0.18 s (means ± SD); $n = 4$ fields of view from two biological replicates; $P = 0.23$]. Meanwhile, nIRCat signals exhibited a wider diversity of decay kinetics [$\tau$: FSCV = 0.51 ± 0.08 s versus nIRCats = 2.43 ± 0.24 s (means ± SD); $n = 4$ fields of view from two biological replicates; $P = 0.0002$). A subset of ROIs exhibited decay time constants that overlapped with, or were faster than, those of FSCV signals (Fig. 2, H and I).

We next evaluated the ability of nIRCats to detect DA in the presence of DA receptor drugs. First, using in vitro solution phase experiments (without biological tissue), we found that nIRCat fluorescence intensity was not modulated by exposure to 1 μM concentration of D2 receptor (D2R) antagonists sulpiride and haloperidol, the D2R agonist quinpirole, or the D1R antagonist SCH 23390 (Fig. 3A). Furthermore, with these in vitro solution phase experiments, we showed that DA-induced nIRCat fluorescence signals were not altered in the presence of these same drugs. These data confirmed that nIRCats retained their functionality in the presence of drugs that serve as DA receptor (DAR) agonists and antagonists (Fig. 3A).

We next moved to brain slice where presynaptic DA autoreceptors are known to play a critical role in regulating DA release. In the dorsal striatum of acute slices from $n = 3$ biological replicates, we found that a D2R agonist suppressed nIRCat transients while a D2R antagonist enhanced them (Fig. 3B). Application of quinpirole (1 μM) suppressed nIRCat fluorescent transients in response to single-pulse electrical stimulation, which recovered following 15-min drug washout (Fig. 3, C and D). Conversely, application of sulpiride (1 μM) significantly increased nIRCat $\Delta F/F$ (Fig. 3, E and F). The effects of these agonists and antagonists were present in ex vivo brain tissue, while they were absent in in vitro solution phase experiments above. Our results are therefore consistent with the powerful inhibition of presynaptic DA release by the D2R agonist quinpirole and the facilitation of presynaptic DA release by the D2R antagonist sulpiride.

Optical recording capability and nanoscale size of nIRCats enables investigation of DA dynamics and pharmacological manipulation with higher spatial resolution than can be achieved using other tools. Therefore, we next examined the effects of quinpirole and sulpiride on individual ROIs (see Materials and Methods). We also used an intermediate dose to provide greater information about differential dose response. We again used electrical stimulation in the dorsal striatum to drive DA release and compared the effect of quinpirole before and after bath application of the drug. We focused on ROIs 4 μm or smaller to capture most of the ROIs while excluding the long tail of larger ROIs that are likely to contain many dopaminergic synapses (Fig. 2, F and G). Averaging all active ROIs 4 μm or smaller, a high (1 μM) concentration of quinpirole yielded post-drug to pre-drug $\Delta F/F$ amplitude ratio of 0.48 ± 0.35 (Fig. 4, A and B). A lower concentration of quinpirole (0.25 μM) resulted in an amplitude ratio of 0.91 ± 0.36 (means ± SD of $n = 150$ ROIs identified within the field of view; Fig. 4, A and B). We repeated the experiment and analysis with bath application of sulpiride (1 μM) and observed a sulpiride-induced amplitude ratio of 2.34 ± 1.3 (means ± SD of $n = 150$ ROIs within field of view; Fig. 4, D and E).

Analyses of individual ROIs (all smaller than 4 μm) revealed heterogeneity in ROI responses upon bath application of either quinpirole or sulpiride. Notably, application of quinpirole preferentially suppressed ROIs that exhibited higher $\Delta F/F$ before application of the

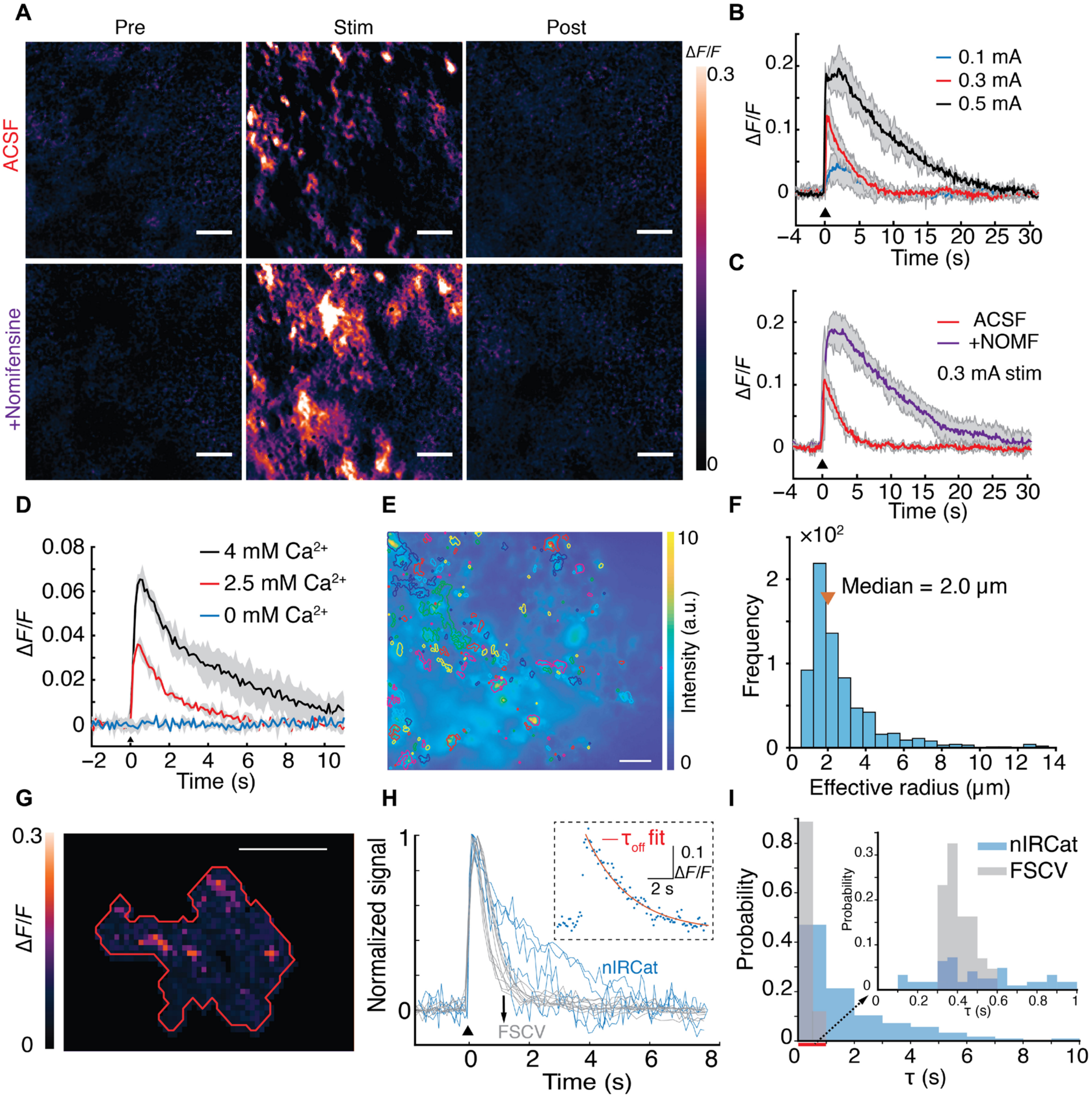

**Fig. 2. Imaging and spatiotemporal analysis of DA release evoked by electrical stimulation in striatal tissue.** (**A**) Repeat images of the same field of view and ΔF/F of nIRCat signal after electrical stimulation of 0.3 mA in standard ACSF (top) and in ACSF and 10 μM nomifensine (bottom, +Nomifensine). Three example still frames are presented: "pre" is before electrical stimulation is applied, "stim" represents frame corresponding to peak ΔF/F following stimulation, and "post" is a frame after nIRCat fluorescence has returned to baseline. Scale bars, 10 μm. (**B**) Nanosensor fluorescence modulation scaled with single-pulse electrical stimulation amplitudes. Field-of-view mean traces and SD bands are presented for three stimulation amplitudes of 0.1, 0.3, and 0.5 mA. (**C**) Time traces of ΔF/F for 0.3-mA single-pulse electrical stimulation in standard ACSF (red) and in ACSF and 10 μM nomifensine (purple, +NOMF). Mean traces with SD bands are presented. (**D**) nIRCat ΔF/F responses are abolished in 0 mM $Ca^{2+}$ ACSF and vary with extracellular ($Ca^{2+}$). (**E**) A single frame from a time series gathered in the dorsomedial striatum showing the entire field of view, overlaid with regions of interest (ROIs) identified using per-pixel ΔF/F stack projections of nIRCat fluorescence modulation (see Materials and Methods). Color bar represents nIRCat labeling fluorescence intensity. Scale bar, 20 μm. (**F**) Frequency histogram of ROI sizes depicted in (E), exhibiting a log-normal distribution with a median ROI size of 2 μm. (**G**) A higher magnification view of an ROI with an effective radius of 5 μm. Maximum ΔF/F projection of the ROI shows the presence of smaller fluorescence hotspots within the ROI. Scale bar, 5 μm. (**H**) Overlay of representative normalized FSCV (gray) and nIRCat (blue) traces showing that nIRCat ROI signals exhibit heterogeneity in decay kinetics. Inset: An example of nIRCat experimental data (blue dots) fitted to first-order decay kinetics (red line) to compute decay time constants (τ). (**I**) Normalized frequency histogram of τs computed from FSCV and nIRCat individual ROI time traces. Data from $n = 4$ fields of view representing $n = 2$ biological replicates were pooled. Medians of each distribution: $\tau = 1.1$ s (nIRCats) and $\tau = 0.4$ s (FSCV).

drug [Pearson correlation of $r = -0.21$ ($P = 0.01$) for 0.25 μM data and $r = -0.17$ ($P = 0.03$) for 1 μM data in Fig. 4C]. Additional quinpirole wash-on results are presented in figs. S6 (A to C) and S9. Conversely, our analysis showed that application of sulpiride enhanced nIRCat response in ROIs that had lower ΔF/F before application of the drug [Pearson correlation of $r = -0.53$ ($P < 0.0001$); Fig. 4F] (see additional data in fig. S6, D and F). Our work uncovers a statistically significant correlation between an ROI's pre-drug ΔF/F amplitude and its post-drug response. It is possible that the observed heterogeneity in ROI responses maps onto variation in D2 autoreceptor

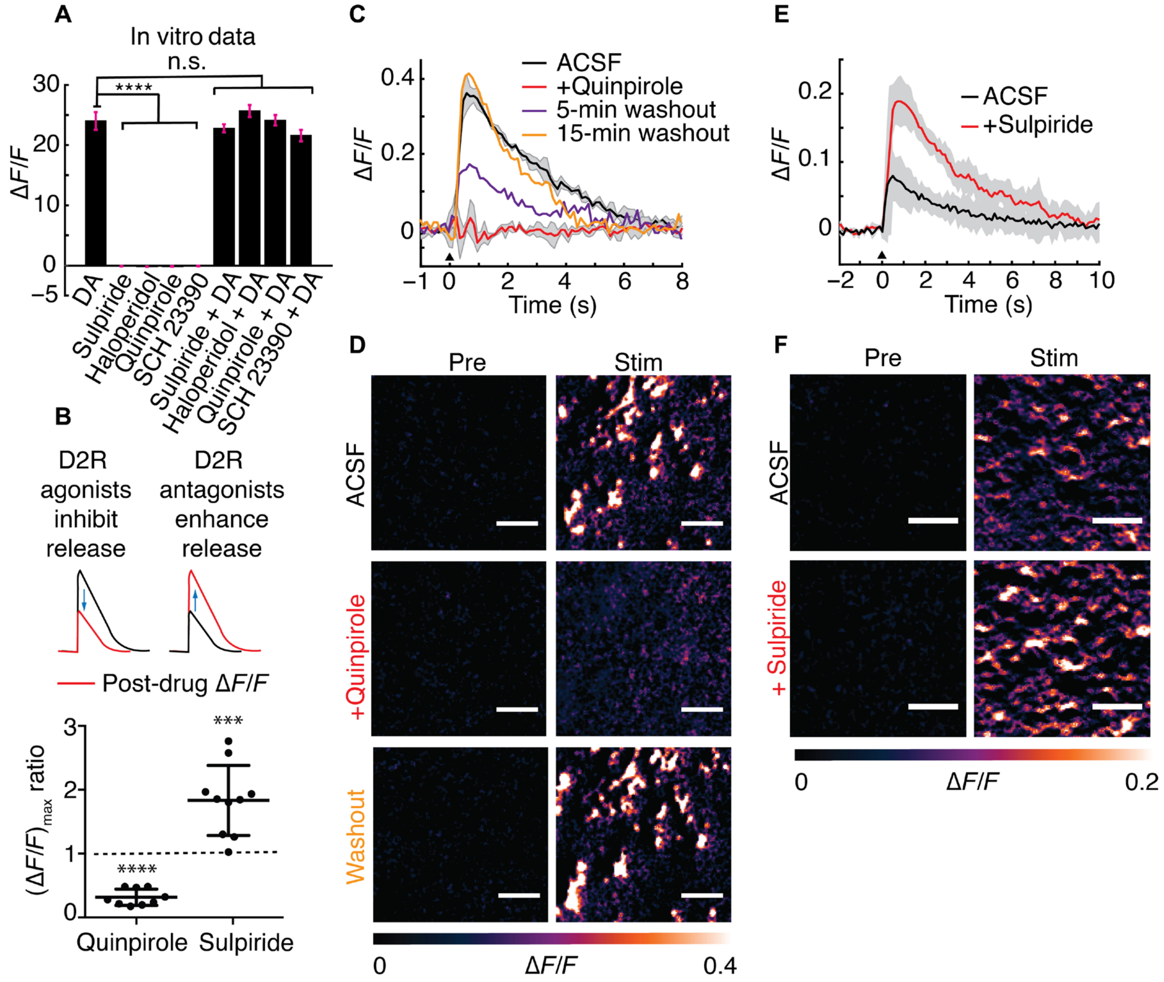

**Fig. 3. Imaging DA release in the presence of DA receptor agonists and antagonists.** (**A**) In vitro solution phase maximal Δ*F*/*F* (amplitude change at ~1128 nm) of nIRCat in the presence of 100 μM DA; the D2R antagonists sulpiride and haloperidol; D2R agonist quinpirole, and D1R antagonist SCH 23390; and drugs and DA. The addition of 1 μM drug quantities did not induce nIRCat fluorescence modulation in the absence of DA (****$P < 0.0001$ compared to DA Δ*F*/*F*). Subsequent addition of DA to drug-incubated nIRCat solutions produced Δ*F*/*F* responses indistinguishable from DA-only responses. Error bars represent SDs from $n = 3$ measurements. n.s., not significant. (**B**) Top: A schematic of the effect of D2R agonist and antagonist drugs on DA release. Bottom: Quinpirole suppressed nIRCat fluorescence modulation (****$P < 0.0001$), whereas sulpiride facilitated nIRCat fluorescence (***$P = 0.001$) in $n = 3$ biological replicates. Individual data point represents $(\Delta F/F)_{\max}$ ratio of the average trace collected in same field of view (post-/pre-drug application). (**C** and **D**) In brain slice, quinpirole (1 μM) suppressed nIRCat fluorescence modulation in response to a single-pulse electrical stimulation (0.5 mA, 3 ms; red trace) compared to pre-drug ACSF (black trace) but recovered following drug washout (purple and orange traces). (**E** and **F**) Sulpiride (1 μM) enhanced nIRCat fluorescence modulation in response to single-pulse electrical stimulation, yielding brighter nIRCat Δ*F*/*F* hotspots compared to drug-free ACSF. Scale bars, 10 μm. All error bands in (C) and (E) represent SD from the mean trace.

expression and/or function (*37*–*40*), but further characterization will be necessary to confirm this hypothesis.

### Imaging of optogenetically evoked DA release in striatal tissue

To further confirm that striatal nIRCat nanosensor signals were reporting DA release, we compared channelrhodopsin (ChR2) stimulation of cortical glutamatergic and nigrostriatal dopaminergic terminals in the dorsal striatum. Acute striatal brain slices were prepared from mice virally transfected to express the light-sensitive cation channel ChR2 in either glutamatergic terminals of the striatum [targeted by viral injection in the frontal cortices (ChR2-GLU); Fig. 5A and fig. S7, A and B] or dopaminergic terminals [targeted by viral injection in the midbrain in DAT-Cre mice (ChR2-DA); Fig. 5C and fig. S7C]. Upon optical stimulation of ChR2-DA terminals with a 473-nm laser (five pulses at 25 Hz, 1 mW/mm$^2$) in the dorsal striatum, we observed significant fluorescence modulation of nIRCat signal (Fig. 5D and movie S2). In contrast, when optogenetic stimulation was targeted at cortical glutamatergic terminals in the striatum, fluorescent nIRCat signals did not rise above baseline fluctuation. Notably, we could confirm in control experiment that optogenetic stimulation of cortical glutamatergic terminals was able to evoke excitatory postsynaptic currents in striatal MSNs (Fig. 5B, inset, and fig. S7, D and E).

Returning to ChR2-DA stimulation, we next varied the number of stimulation pulses (5-ms pulse duration, 25 Hz, 1 mW/mm$^2$) and observed scaling in nIRCat Δ*F*/*F* amplitude from 1 to 10 pulses ($P = 0.005$) and trend level differences between 1 and 5 pulses ($P = 0.0645$) and between 5 and 10 pulses ($P = 0.086$; Fig. 5E). When we varied the pulse frequency while holding the number of pulses

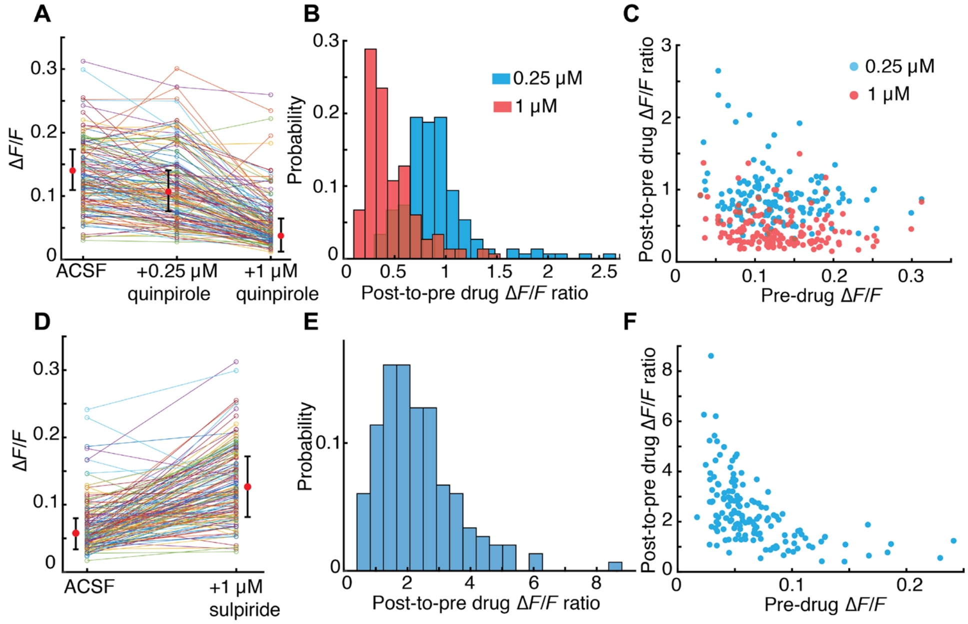

**Fig. 4. Effects of quinpirole and sulpiride on nIRCat response at the level of ROIs (4 μm or smaller).** (**A**) Δ*F*/*F* of ROIs in ACSF and in ACSF with 0.25 μM and 1 μM of quinpirole. Each Δ*F*/*F* data point corresponding to an ROI is an average from $n = 3$ stimulation repeats. (**B**) Distribution of nIRCat response attenuation upon the addition of 0.25 μM (blue) or 1 μM (red) quinpirole for ROIs in (A). (**C**) Scatter plot of response to drug versus pre-drug Δ*F*/*F* amplitude for data in (A). (**D**) Δ*F*/*F* of ROIs in ACSF and following the addition of 1 μM of sulpiride. Each Δ*F*/*F* data point corresponding to an ROI is an average from $n = 3$ stimulation repeats. (**E**) Distribution of post-to-pre drug Δ*F*/*F* ratio for data in (D). (**F**) Scatter plot of response to drug versus pre-drug Δ*F*/*F* amplitude for data in (D). For (A) and (D), means and error bars (SD) are presented next to each distribution.

constant at five, we observed scaling with significant differences detectable between 1 and 10 Hz ($P = 0.036$). The amplitude difference between 10 and 25 Hz did not reach significance ($P = 0.179$; Fig. 5F). In single-pulse experiments in which we varied pulse width, nIRCat fluorescence responses scaled with pulse duration. This effect was significant when comparing 2 to 5 ms ($P = 0.002$), but the difference from 5 to 10 ms did not reach significance ($P = 0.055$; Fig. 5G).

Last, we tested the effect of dopaminergic pharmacological agents on optogenetically evoked DA release (ChR2-DA). Bath application of quinpirole (1 μM) powerfully suppressed nIRCat fluorescence ($P < 0.0001$), and this effect was reversed after drug washout (Fig. 5H). Consistent with results from electrical stimulation, optogenetic stimulation also showed that quinpirole preferentially suppressed the most active ROIs (fig. S8). Nomifensine (10 μM) enhanced nIRCat signal decay time, consistent with the predicted slowing of DA clearance from the ECS (fig. S9).

## DISCUSSION

To understand how neuromodulation alters the plasticity and activity of distinct populations of neurons, there is a need for new optical tools that can measure the extracellular dynamics of neuromodulator release and reuptake at spatiotemporal resolution commensurate with methods used to record neural activity (e.g., electrophysiology and calcium imaging). Here, we demonstrated the feasibility of using a nongenetically encoded fluorescent sensor, nIRCat, to enable optical detection of catecholamine release and reuptake with subsecond temporal and micrometer spatial resolution. We used electrical and optogenetic methods in striatal brain tissue to demonstrate that nIRCat fluorescent signals faithfully report evoked DA release and pharmacologically induced changes in DA dynamics.

We focused nIRCat imaging experiments within the dorsal striatum, a region that receives dense dopaminergic innervation and negligible norepinephrinergic innervation (*29*). Therefore, while nIRCats may not be selective for DA over NE, nIRCats effectively function as a DA sensor within the context of the striatum. Given that striatal DA regulates fundamental processes, including motor function, motivation, and learning, nIRCats represent an important addition to the neuroscience investigative toolkit. Furthermore, of the biogenic amines present in invertebrate species (DA, tyramine, octopamine, serotonin, and histamine), we demonstrated in vitro that nIRCats are exclusively sensitive to DA. Hence, for invertebrate species such as drosophila, we predict that nIRCats may serve as selective and highly sensitive DA sensors throughout the brain.

While other tools are emerging to optically report DA fluctuations via cell surface–engineered proteins (*41*, *42*), nIRCats are likely to fulfill a niche among currently available methods for detecting DA neurotransmission because of their unique nIR fluorescence, the fact that they do not rely on genetic delivery and expression, their relative ease of deployment, and their functionality in the presence of pharmacological DA receptor ligands. This is in contrast to receptor-based fluorescent sensors, which currently cannot report on endogenous DA dynamics in the presence of ligands to the engineered receptor but do exhibit selectivity for DA over NE (*41*, *42*). Furthermore, the synthetic nature of nIRCats eliminates concern about potential G protein–coupled receptor–mediated residual signaling that may be present in protein-based optical probes. nIRCats also offer spatial advantages over FSCV, and our initial experiments suggest that the temporal resolution of the nIRCat signal can be comparable to that of FSCV. nIRCat fluorescence decay profiles exhibit a wider temporal range than that observed from FSCV data and included a significant number of ROIs that showed seconds-long

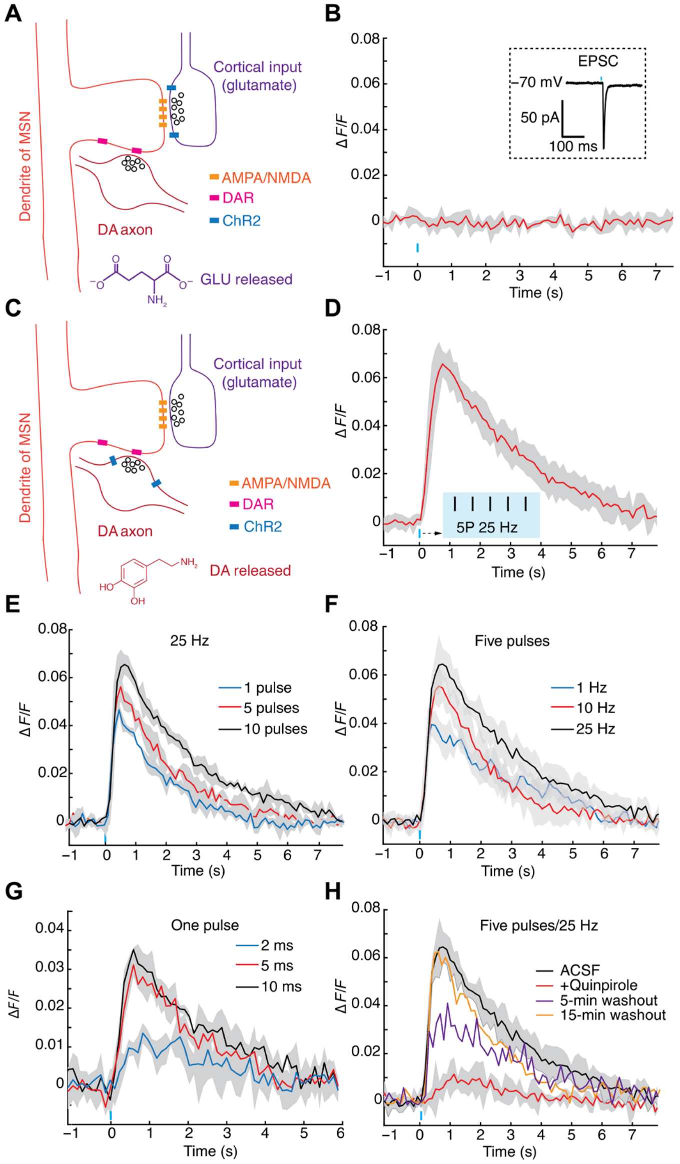

**Fig. 5. nIRCat detection of striatal DA release evoked by optogenetic stimulation.** (**A**) Schematic of ChR2 expression in cortical glutamatergic terminals synapsing in the dorsal striatum. AMPA, α-amino-3-hydroxyl-5-methyl-4-isoxazolepropionate; NMDA, *N*-methyl-D-aspartate; DAR, DA receptor. (**B**) No nIRCat fluorescence modulation was observed after stimulation of glutamatergic terminals. Inset: GLU release was confirmed by excitatory postsynaptic current (EPSC) on MSN. (**C**) Schematic of ChR2 expression in nigrostriatal dopaminergic terminals of the dorsal striatum. (**D**) Stimulation of dopaminergic terminals resulted in nIRCat fluorescence modulation. Stimulation protocol in (B) and (D) was five pulses (5P) at 25 Hz and a power flux of 1 mW/mm$^2$, and each pulse had a duration of 5 ms. (**E**) nIRCat Δ*F*/*F* in response to increasing number of pulses delivered at 25 Hz (5-ms pulse duration). (**F**) nIRCat Δ*F*/*F* in response to increasing pulse frequency (1, 10, and 25 Hz) of five pulses. Each pulse had a duration of 5 ms. (**G**) nIRCat Δ*F*/*F* in response to single pulses of 2-, 5-, and 10-ms duration. (**H**) Bath application of 1 μM of quinpirole suppresses DA release and results in depressed nIRCat Δ*F*/*F*. Drug washout rescues DA release and nIRCat Δ*F*/*F*. All error bands represent SD from the mean trace.

time constants in addition to time constants faster than those measured by FSCV. It is debatable whether these results capture the unique spatial properties of specific striatal ROIs or are related to tool differences alone. nIRCats should also sample catecholamine concentration at a smaller spatial scale compared to FSCV. Each distributed nIRCat construct can act as a probe within the ECS and therefore yield a "higher resolution" picture of neuromodulatory dynamics. Future experiments will investigate how the heterogeneity of nIRCat signals (amplitude, kinetics, and modulation by drugs) relates to structural and functional properties at DA terminals and within the ECS. We predict that new optical tools for measuring DA dynamics with high spatial resolution will enable new insights into the regulation of DA release and reuptake at the level of individual synapses (*43*–*45*).

Furthermore, we see potential for future expansion of a larger family of SWNT-based nIR nanosensors (nIRNSs) similar to nIRCats for multiple neurochemical imaging applications. Several lines of evidence illustrate their future potential. First, nIRNSs are easily functionalized with a wide range of synthetic molecular recognition moieties, affording fine control of their surface functional elements and their interactions with the local chemical environment (*22*, *46*, *47*). SWNT fluorescence can be finely tuned to monochromatic emission in the nIR II window (1000 to 1700 nm) by controlling the SWNT chirality (*48*). This chirality-dependent fluorescence in the nIR II window provides further avenues for simultaneously designing color-specific responses to multiple molecular analytes, thereby affording synthesis of ratiometric and multiplexed analyte imaging platforms, as we have shown previously (*49*). Second, SWNT-based nanosensors rely on nIR fluorescence, which greatly reduces the impact of tissue scattering in the emission window and therefore may enable through-cranium imaging (*25*). nIRNSs are compatible with multiphoton imaging with an excitation of 1600 nm (*50*) and, as such, could permit nanoscale imaging of intact neuronal structures pending parallel developments in all-infrared microscopy, as has been shown with visible wavelength-emitting fluorophores (*51*). Third, nIRNSs exhibit robust nonphotobleaching photostability, allowing their use in long-term imaging experiments (*52*). Fourth, because nIRNSs are not genetically encoded, they could enable use in species where gene delivery and protein expression are intractable, time-consuming, or undesirable. Last, the nanosecond-scale binding kinetics and nanoscale dimensions of nIRNSs are likely to enable generation of other neuromodulator nanosensors with improved temporal and spatial resolution. In summary, nIRCats are versatile catecholamine probes amenable to multiplexing with existing tools for concurrent investigation of dopaminergic neuromodulation with other core mechanisms of brain function.

## MATERIALS AND METHODS

### Nanosensor synthesis

(GT)$_6$ oligonucleotides were purchased from Integrated DNA Technologies (standard desalting). HiPco SWNTs were purchased from NanoIntegris (batch no. HR27-104). (GT)$_6$-SWNT colloidal suspension (nIRCat) was prepared by mixing 1 mg of (GT)$_6$ and 1 mg of SWNTs in 1 ml of a 100 mM NaCl solution. The solution was bath-sonicated (Branson Ultrasonic 1800) and probe tip-sonicated (Cole-Parmer Ultrasonic Processor, 3-mm tip in diameter, 5 W power) for 10 min each in an ice-bath. The sonicated solution was incubated at room temperature for 30 min. The product was subsequently centrifuged at 16,000*g* (Eppendorf 5418) for 90 min to remove unsuspended SWNT bundles and amorphous carbon, and the supernatant was recovered for characterization and use. Each nanosensor suspension was stored at 4°C until use.

### Nanosensor characterization

To characterize nIRCats after synthesis, the full visible and nIR absorption spectrum was taken for each nanosensor batch (UV-VIS-nIR spectrophotometer, Shimadzu UV-3600 Plus) or UV-VIS (Thermo Fisher Scientific Genesys 20). SWNT concentrations of as-made nanosensor batches were determined using absorbance at 632 nm (UV-VIS) with an extinction coefficient of $\varepsilon = 0.036$ (mg/liter)$^{-1}$ cm$^{-1}$. Full spectrum absorbance measurements were made with UV-VIS-nIR after dilution to an SWNT concentration of 5 mg/liter in 100 mM NaCl. For fluorescence spectroscopy, each sensor batch was diluted to a working concentration of 5 mg/liter in 100 mM NaCl, and aliquots of 198 μl were placed in each well of a 96-well plate (Corning). Fluorescence measurements were obtained with a 20× objective on an inverted Zeiss microscope (Axio Observer D1) coupled to a Princeton Instruments spectrograph (SCT 320) and a liquid nitrogen–cooled Princeton Instruments InGaAs linear array detector (PyLoN-IR). A 721-nm laser (Opto Engine LLC) was used as the excitation light source for all characterization experiments.

### Neurotransmitter library and dopamine receptor drug screening

For neurotransmitter response screens, we collected the nIR fluorescence spectrum from 198 μl aliquots of nanosensor (an SWNT concentration of 5 mg/liter) before and after the addition of 2 μl of 10 mM solutions of each analyte neurotransmitter (for a 100 μM final analyte concentration in each well of a 96-well plate). All neurotransmitter analytes were purchased from Sigma-Aldrich. Neurotransmitter analytes were incubated for 5 min before taking post-analyte fluorescence measurements. Responses were calculated for the integrated fluorescence count as $\Delta F/F_0 = (F - F_0)/F_0$, where $F_0$ is the total fluorescence before analyte addition and $F$ is the total fluorescence after analyte addition or for peak fluorescence change corresponding to the (*9*, *4*) SWNT chirality (center wavelength, ~1128 nm). All measurements were made in triplicate. Reported results are means ± SD of the triplicate measurements. All nIRCat nanosensor batches were tested for catecholamine responses before use for tissue catecholamine imaging. DA receptor drugs were purchased from Tocris Bioscience (quinpirole and sulpiride), Abcam (SCH 23390), and Sigma-Aldrich (haloperidol). nIRCat fluorescence modulation to DRDs was measured after the addition of 1 μM drug quantities (final concentration in well) in each well. Post-drug fluorescence spectra were taken after 5-min drug incubation. To measure nIRCat response to DA in the presence of drugs, DA aliquots were added to each drug-incubated well to obtain 100 μM of DA, and post-DA fluorescence spectra were taken after an additional 5-min incubation period.

### Nanosensor reversibility testing

A 1.5 glass coverslip was functionalized with 3-aminopropyltriethoxysilane (APTES; Sigma-Aldrich) by soaking in 10% APTES in ethanol for 5 min. The coverslip was then rinsed with deionized water and left to dry. The coverslip was then fixed onto an ibidi sticky-Slide VI 0.4 forming six microfluidic channels. First, 100 μl of phosphate-buffered saline (PBS) was pipetted through a channel. Next, the channel was filled with 50 μl of a solution (5 mg/liter) of nIRCats and left to incubate at room temperature for 5 min. The channel was rinsed using three 50 μl of PBS washes, keeping the channel filled with solution at all times. The surface-immobilized nIRCats in PBS were imaged on an epifluorescence microscope with an excitation of 721 nm and a Ninox VIS-SWIR 640 camera (Raptor). One end of the flow channel was connected to a syringe pump (Harvard Apparatus) using Luer lock fittings. Before the start of image acquisition, the opposite flow reservoir was filled with PBS, and the pump was set to refill mode at a volumetric flow rate of 40 μl min$^{-1}$. Once the liquid in the reservoir was depleted, 40 μl of 10 μM DA in PBS was added. The process was repeated using alternating additions of 80 μl of PBS washes and 40 μl of DA solution.

### Acute slice preparation and nanosensor labeling

Mice were C57BL/6 strain (60 days old), and both male and female mice were used. Mice were group-housed after weaning at postnatal day 21 (P21) and kept with nesting material on a 12:12 light cycle. All animal procedures were approved by the University of California Berkeley Animal Care and Use Committee. Acute brain slices were prepared using established protocols (*32*). Briefly, mice were deeply anesthetized via intraperitoneal injection of ketamine/xylazine cocktail, and transcardial perfusion was performed using ice-cold cutting buffer (119 mM NaCl, 26.2 mM $NaHCO_3$, 2.5 mM KCl, 1 mM $NaH_2PO_4$, 3.5 mM $MgCl_2$, 10 mM glucose, and 0 mM $CaCl_2$), after which the brain was rapidly extracted. The cerebellum and other connective tissues were trimmed using a razor blade, and the brain was mounted onto the cutting stage of a vibratome (Leica VT1200 S). Coronal slices (thickness, 300 μm) including the dorsal striatum were prepared. Slices were incubated at 37°C for 60 min in oxygen-saturated ACSF (119 mM NaCl, 26.2 mM $NaHCO_3$, 2.5 mM KCl, 1 mM $NaH_2PO_4$, 1.3 mM $MgCl_2$, 10 mM glucose, and 2 mM $CaCl_2$) before use. Slices were then transferred to room temperature for 30 min before starting imaging experiments and were maintained at room temperature for the remainder of experimentation.

For nanosensor labeling, slices were transferred into a small volume brain slice incubation chamber (Scientific Systems Design Inc., AutoMate Scientific) and kept under oxygen-saturated ACSF (total volume, 5 ml). One hundred microliters of nIRCat nanosensor (100 mg/liter) was added to the 5-ml volume, and the slice was incubated in this solution for 15 min. The slice was subsequently recovered and rinsed in oxygen-saturated ACSF to wash off nIRCats that did not localize into the brain tissue. The rinsing step was performed by transferring the slice through three wells of a 24-well plate (5 s in each well), followed by transfer to the recording chamber with ACSF perfusion for a 15-min equilibration period before starting the imaging experimentation. All imaging experiments were performed at 32°C.

### Acute slice preparation for FSCV recording

Acute slices were prepared as described previously. Extracellular DA concentration evoked by local electrical stimulation was monitored with FSCV at carbon fiber microelectrodes (CFMs) using a Millar voltammeter. CFMs were ~7 μm in diameter encased in glass capillary pulled to form a seal with the fiber and cut to final tip length of 70 to 120 μm. The CFM was positioned ~100 μm below the tissue surface at a 45° angle. A triangular waveform was applied to the CFM scanning from −0.7 to +1.3 V and back, against Ag/AgCl reference electrode at a rate of 800 V/s. Evoked DA transients were sampled at 8 Hz, and data were acquired at 50 kHz using AxoScope 10.5 (Molecular Devices). Oxidation currents evoked by electrical stimulation were converted to DA concentration from post-experimental calibrations. Recorded FSCV signals were identified as DA by comparing oxidation (+0.6 V) and reduction (−0.2 V) potential peaks from experimental voltammograms with currents recorded during calibration with 2 μM DA dissolved in ACSF. For stimulation, a bipolar stimulation electrode (FHC CBAEC75) was positioned on top of the brain slice and approximately 100 μm away from the CFM. Following 30-min slice equilibration in the recording chamber, DA release was evoked using a square pulse (pulse amplitude, 0.3 mA; pulse duration, 3 ms) controlled by an ISO-Flex stimulus isolator (A.M.P.I) and delivered out of phase with the voltammetric scans. Stimulation was repeated three times. To compare FSCV and nIRcat data, each signal was normalized against its peak value [$(DA)_{max}$ or $(\Delta F/F)_{max}$] and coaligned at stimulation time. Latency to peak was computed as $t_{peak} - t_{stim}$, where $t_{peak}$ is the time at which peak signal is attained, and $t_{stim}$ is time of stimulation. Decay time constants ($\tau$) were computed from model fits to a first-order decay process.

### Microscope construction and slice imaging

Ex vivo slice imaging was performed with a modified upright epifluorescent microscope (Olympus, Sutter Instruments) mounted onto a motorized stage. Nanosensor excitation was supplied by a 785-nm CW DPSS (continuous-wave diode-pumped solid-state) laser with adjustable output power to a maximum of 300 mW and a near TEM00 top hat beam profile (Opto Engine LLC). The beam was expanded using a Keplerian beam expander composed of two plano-convex lenses ($f$ = 25 and 75 mm; AR coating B, Thorlabs) to a final beam diameter of approximately 1 cm. The beam was passed through a custom fluorescence filter cube [excitation: 800 nm shortpass (FESH0800), dichroic: 900 longpass (DMLP990R), and emission: 900 longpass (FELH0900); Thorlabs] to a 60× Apo objective (numerical aperture, 1.0; working distance, 2.8 mm; water dipping; high nIR transmission; Nikon CFI Apo 60XW nIR). Emission photons collected from the sample were passed through the filter cube, were focused onto a two-dimensional InGaAs array detector [500 to 600 nm: 40% quantum efficiency (QE); 1000 to 1500 nm: >85% QE; Ninox 640, Raptor Photonics], and were recorded using the Micro-Manager Open Source Microscopy Software (*53*). Laser power was adjusted to maximize collected photons and to fill the pixel bit depth on the detector but did not exceed 70 mW at the objective back focal plane. Yellow fluorescent protein (YFP) was imaged by switching the filter cube (U-N41017XL, Olympus) and by using a mercury-vapor lamp (Olympus) for excitation.

### Electrical and optical stimulation–evoked DA imaging with nIR microscopy

For electrical stimulation experiments, a bipolar stimulation electrode was positioned in field of view within the dorsomedial striatum identified using a 4× objective (Olympus XLFluor 4×/340). Using 60× objective, the stimulation electrode was brought into contact with top surface of the brain slice and an imaging field of view was chosen at a nominal distance of 150 μm from the stimulation electrode within the dorsomedial striatum. All stimulation experiments were recorded at video frame rates of 9 frames per second (nominal), and single-pulse electrical stimulations were applied after 200 frames of baseline were acquired. Each video acquisition lasted 600 frames. Stimulation amplitudes were staggered, and each stimulation amplitude was repeated three times within a field of view. Slices were allowed to recover for 5 min between each stimulation, with the excitation laser path shuttered. For optogenetic stimulation, a fiber-coupled 473-nm blue laser (Opto Engine LLC DPSS) was positioned in close proximity to the brain slice using a micromanipulator. Expression of ChR2 was confirmed via visible fluorescence imaging, and an imaging field of view was chosen in dorsomedial striatum with robust expression level. Stimulation pulses (five pulses, 5-ms duration per pulse at 25 Hz, 1 $mW/mm^2$) were delivered after acquiring 200 baseline frames, and the video acquisition lasted 600 frames at nominal 9 frames per second. Drugs were bath-applied to the imaging chamber through ACSF perfusion. ACSF with 10 μM of nomifensine or 1 μM of each drug was used. When the effect of a drug was needed to be evaluated, stimulation/imaging experiments were carried out with drug-free ACSF in an imaging field of view to collect drug-free data. Normal ACSF was then switched to ACSF prepared with the drug of interest and applied for 10 min before stimulation/imaging experiments resumed.

### Viral transfection of mice for optogenetic stimulation

Adult male and female mice (>P60) were used for all surgeries. Bilateral viral injections were performed using previously described procedures (*54*) at the following stereotaxic coordinates: 1.94 mm from bregma, 0.34 mm lateral from midline, and 0.70 mm vertical from cortical surface for dorsomedial prefrontal cortex (dmPFC) and −3.08 mm from bregma, 1.25 mm lateral from midline, and 4.0 mm vertical from cortical surface for SNc. For glutamatergic corticostriatal axon stimulation experiments, mice were bilaterally injected with 0.5 μl of CAG-ChR2-EYFP (enhanced YFP) virus into dmPFC. For nigrostriatal dopaminergic axon stimulation experiments, DAT-Cre mice were injected with 0.5 μl of DIO-ChR2-EYFP virus bilaterally. For all optogenetic experiments, we waited at least 3 weeks from viral injection to experimental stimulation to allow for sufficient ChR2 gene expression.

To confirm that DA neurons were transfected with ChR2 in animals used for optogenetic DA stimulation experiments, we perfused DAT-Cre mice that had been injected into the SNc with Cre-dependent ChR2-EYFP virus with 4% paraformaldehyde in PBS and post-fixed brains overnight. Coronal sections that included the injection site (SNc) and imaging site (dorsal striatum) were cut at 50 μM and immunolabeled using antibody against tyrosine hydroxylase [TH (1:1000); rabbit anti-TH, Millipore], the rate-limiting enzyme for catecholamine synthesis. Goat anti-rabbit DyLight 594 secondary antibody (1:1000; Invitrogen) was used to visualize TH. Image acquisition was performed on a Zeiss Axio ScanZ.1 using a 5× objective.

### Image processing and data analysis of nIRCat fluorescence response

Raw movie files were processed using a custom-built MATLAB program (https://github.com/jtdbod/Nanosensor-Brain-Imaging). Briefly, for each raw movie stack (600 frames), a per-pixel $\Delta F/F$ defined as $(F - F_0)/F_0$ was calculated using the average intensity for the first 5% of frames as $F_0$, and $F$ represents the dynamic fluorescence intensity at each pixel. ROIs were identified by calculating a median filter convolution and then performing thresholding using Otsu's method to identify ROIs with strong fluorescence modulation over background, followed by a morphological dilation operation. $\Delta F/F$ traces were then calculated for each generated ROI by averaging pixel values over the ROI. ROI sizes were computed using the measured pixel area and by approximating each as a circle to calculate an equivalent radius.

To compare responses across stimulation amplitudes and bath application of nomifensine, mean results were obtained as follows: First, all identified ROIs from a field of imaging were averaged. Mean traces were further averaged over different fields of view within the same slice and across slices (1 to 2 fields of view per slice and 1 to

2 slices per animal) and then averaged over experimental animals. Decay time constants ($\tau$) were computed by fitting $\Delta F/F$ time traces to a first-order decay process on an ROI basis or field-of-view average basis. Latency to peak was computed as $t_{\mathrm{peak}} - t_{\mathrm{stim}}$, where $t_{\mathrm{peak}}$ is the time at which peak signal is attained and $t_{\mathrm{stim}}$ is time of stimulation. All statistical tests of significance ($P$ values) were computed and reported from unpaired two-tailed $t$ test.

ROI-level analysis of drug washes were computed by generating an ROI mask from one of the triplicate stimulations and then computing $\Delta F/F$ traces using the same ROI mask for all experimental runs (before and after application of drug). Each raw movie file was corrected for translational and rotational drift using StackReg plugin in FIJI and then processed using our custom MATLAB script. We removed all ROIs that were greater than 4 μm in size for subsequent analysis. For each ROI, post-to-pre drug ratios were computed as $(\Delta F/F)_{\mathrm{max\text{-}post\text{-}drug}}/(\Delta F/F)_{\mathrm{max\text{-}pre\text{-}drug}}$. Here, we define $(\Delta F/F)_{\mathrm{max}}$ as the amplitude of nIRCat response in the post-stimulation epoch. Mean values from triplicate stimulation were used to evaluate the ratio.

## SUPPLEMENTARY MATERIALS

Supplementary material for this article is available at http://advances.sciencemag.org/cgi/content/full/5/7/eaaw3108/DC1

Fig. S1. nIRCats are compatible with concentrations and conditions expected in brain tissue.

Fig. S2. Surface-immobilized single nIRCats are reversible upon repeat exposure to DA.

Fig. S3. Brain slice nIRCat loading protocol and schematic of visible and nIR fluorescence microscopy for imaging nIRCats in brain tissue.

Fig. S4. nIRCat imaging in *M. spicilegus* brain tissue.

Fig. S5. Intensity of nIRCat labeling at baseline does not predict site of $\Delta F/F$ hotspots.

Fig. S6. Variability in effect of quinpirole and sulpiride on nIRCat response on spatially segregated ROIs within a field of view.

Fig. S7. Data that confirm targeting of optogenetic stimulation of dopaminergic and glutamatergic inputs to the striatum.

Fig. S8. Effect of quinpirole on ChR2 evoked nIRCat response at the level of ROIs.

Fig. S9. Nomifensine extends nIRCat response to ChR2 stimulation of dopaminergic terminals in the dorsal striatum.

Movie S1. A representative movie from single-pulse electrical stimulation (0.3 mA) in dorsal striatum.

Movie S2. A representative movie from optogenetic stimulation (five pulses at 25 Hz, 1 mW mm$^2$) in dorsal striatum.

## REFERENCES AND NOTES

1. B. A. Anderson, H. Kuwabara, D. F. Wong, E. G. Gean, A. Rahmim, J. R. Brašić, N. George, B. Frolov, S. M. Courtney, S. Yantis, The role of dopamine in value-based attentional orienting. *Curr. Biol.* **26**, 550–555 (2016).
2. M. V. Solanto, Dopamine dysfunction in AD/HD: integrating clinical and basic neuroscience research. *Behav. Brain Res.* **10**, 65–71 (2002).
3. J. Y. Cohen, S. Haesler, L. Vong, B. B. Lowell, N. Uchida, Neuron-type-specific signals for reward and punishment in the ventral tegmental area. *Nature* **482**, 88–88 (2012).
4. N. Eshel, J. Tian, M. Bukwich, N. Uchida, Dopamine neurons share common response function for reward prediction error. *Nat. Neurosci.* **19**, 479–486 (2016).
5. J. D. Berke, What does dopamine mean? *Nat. Neurosci.* **21**, 787–793 (2018).
6. E. E. Steinberg, R. Keiflin, J. R. Boivin, I. B. Witten, K. Deisseroth, P. H. Janak, A causal link between prediction errors, dopamine neurons and learning. *Nat. Neurosci.* **16**, 966–973 (2013).
7. A. A. Hamid, J. R. Pettibone, O. S. Mabrouk, V. L. Hetrick, R. Schmidt, C. M. Vander Weele, R. T. Kennedy, B. J. Aragona, J. D. Berke, Mesolimbic dopamine signals the value of work. *Nat. Neurosci.* **19**, 117–126 (2015).
8. J. D. Salamone, M. Correa, The mysterious motivational functions of mesolimbic dopamine. *Neuron* **76**, 470–485 (2012).
9. J. T. Dudman, J. W. Krakauer, The basal ganglia: From motor commands to the control of vigor. *Curr. Opin. Neurobiol.* **37**, 158–166 (2016).
10. J. Lotharius, P. Brundin, Pathogenesis of parkinson's disease: Dopamine, vesicles and α-synuclein. *Nat. Rev. Neurosci.* **3**, 932–942 (2002).
11. J. J. Weinstein, M. O. Chohan, M. Slifstein, L. S. Kegeles, H. Moore, A. Abi-Dargham, Pathway-specific dopamine abnormalities in schizophrenia. *Biol. Psychiatry* **81**, 31–42 (2017).
12. N. D. Volkow, J. S. Fowler, G.-J. Wang, J. M. Swanson, Dopamine in drug abuse and addiction: Results from imaging studies and treatment implications. *Mol. Psychiatry* **9**, 557–569 (2004).
13. J. D. Clements, R. A. Lester, G. Tong, C. E. Jahr, G. L. Westbrook, The time course of glutamate in the synaptic cleft. *Science* **258**, 1498–1501 (1992).
14. P. Greengard, The neurobiology of slow synaptic transmission. *Science* **294**, 1024–1030 (2001).
15. L. F. Agnati, M. Zoli, I. Strömberg, K. Fuxe, Intercellular communication in the brain: Wiring versus volume transmission. *Neuroscience* **69**, 711–726 (1995).
16. M. Zoli, C. Torri, R. Ferrari, A. Jansson, I. Zini, K. Fuxe, L. F. Agnati, The emergence of the volume transmission concept. *Brain Res. Rev.* **26**, 136–147 (1998).
17. M. E. Rice, S. J. Cragg, Dopamine spillover after quantal release: Rethinking dopamine transmission in the nigrostriatal pathway. *Brain Res. Rev.* **58**, 303–313 (2008).
18. S. J. Cragg, M. E. Rice, DAncing past the DAT at a DA synapse. *Trends Neurosci.* **27**, 270–277 (2004).
19. J. K. Dreyer, K. F. Herrik, R. W. Berg, J. D. Hounsgaard, Influence of phasic and tonic dopamine release on receptor activation. *J. Neurosci.* **30**, 14273–14283 (2010).
20. E. Marder, Neuromodulation of neuronal circuits: Back to the future. *Neuron* **76**, 1–11 (2012).
21. P. V. Jena, D. Roxbury, T. V. Galassi, L. Akkari, C. P. Horoszko, D. B. Iaea, J. Budhathoki-Uprety, N. Pipalia, A. S. Haka, J. D. Harvey, J. Mittal, F. R. Maxfield, J. A. Joyce, D. A. Heller, A carbon nanotube optical reporter maps endolysosomal lipid flux. *ACS Nano* **11**, 10689–10703 (2017).
22. P. W. Barone, S. Baik, D. A. Heller, M. S. Strano, Near-infrared optical sensors based on single-walled carbon nanotubes. *Nat. Mater.* **4**, 86–92 (2005).
23. J. D. Harvey, P. V. Jena, H. A. Baker, G. H. Zerze, R. M. Williams, T. V. Galassi, D. Roxbury, J. Mittal, D. A. Heller, A carbon nanotube reporter of microRNA hybridization events in vivo. *Nat. Biomed. Eng.* **1**, 0041 (2017).
24. A. G. Beyene, A. A. Alizadehmojarad, G. Dorlhiac, A. M. Streets, P. Král, L. Vuković, M. P. Landry, Ultralarge modulation of single wall carbon nanotube fluorescence mediated by neuromodulators adsorbed on arrays of oligonucleotide rings. *Nano. Lett.* **11**, 6995–7003 (2018).
25. G. Hong, S. Diao, J. Chang, A. L. Antaris, C. Chen, B. Zhang, S. Zhao, D. N. Atochin, P. L. Huang, K. I. Andreasson, C. J. Kuo, H. Dai, Through-skull fluorescence imaging of the brain in a new near-infrared window. *Nat. Photonics* **8**, 723–730 (2014).
26. J. Zhang, M. P. Landry, P. W. Barone, J.-H. Kim, S. Lin, Z. W. Ulissi, D. Lin, B. Mu, A. A. Boghossian, A. J. Hilmer, A. Rwei, A. C. Hinckley, S. Kruss, M. A. Shandell, N. Nair, S. Blake, F. Şen, S. Şen, R. G. Croy, D. Li, K. Yum, J.-H. Ahn, H. Jin, D. A. Heller, J. M. Essigmann, D. Blankschtein, M. S. Strano, Molecular recognition using corona phase complexes made of synthetic polymers adsorbed on carbon nanotubes. *Nat. Nanotechnol.* **8**, 959–968 (2013).
27. S. Kruss, M. P. Landry, E. Vander Ende, B. M. A. Lima, N. F. Reuel, J. Zhang, J. Nelson, B. Mu, A. Hilmer, M. Strano, Neurotransmitter detection using corona phase molecular recognition on fluorescent single-walled carbon nanotube sensors. *J. Am. Chem. Soc.* **136**, 713–724 (2014).
28. A. G. Beyene, I. R. McFarlane, R. L. Pinals, M. P. Landry, Stochastic simulation of dopamine neuromodulation for implementation of fluorescent neurochemical probes in the striatal extracellular space. *ACS Chem. Nerosci.* **8**, 2275–2289 (2017).
29. C. W. Berridge, B. D. Waterhouse, The locus coeruleus–noradrenergic system: Modulation of behavioral state and state-dependent cognitive processes. *Brain Res. Rev.* **42**, 33–84 (2003).
30. C. R. Gerfen, Synaptic organization of the striatum. *J. Electron Microsc. Tech.* **10**, 265–281 (1988).
31. N. X. Tritsch, B. L. Sabatini, Dopaminergic modulation of synaptic transmission in cortex and striatum. *Neuron* **76**, 33–50 (2012).
32. D. J. Piekarski, J. R. Boivin, L. Wilbrecht, Ovarian hormones organize the maturation of inhibitory neurotransmission in the frontal cortex at puberty onset in female mice. *Curr. Biol.* **27**, 1735–1745.e3 (2017).
33. A. G. Godin, J. A. Varela, Z. Gao, N. Danné, J. P. Dupuis, B. Lounis, L. Groc, L. Cognet, Single-nanotube tracking reveals the nanoscale organization of the extracellular space in the live brain. *Nat. Nanotechnol.* **12**, 238–243 (2017).
34. D. L. Robinson, B. J. Venton, M. L. A. V. Heien, R. M. Wightman, Detecting subsecond dopamine release with fast-scan cyclic voltammetry in vivo. *Clin. Chem.* **49**, 1763–1773 (2003).
35. M. L. A. V. Heien, M. A. Johnson, R. M. Wightman, Resolving neurotransmitters detected by fast-scan cyclic voltammetry. *Anal. Chem.* **76**, 5697–5704 (2004).
36. P. A. Garris, R. M. Wightman, Regional differences in dopamine release, uptake, and diffusion measured by fast-scan cyclic voltammetry. *Neuromethods Voltammetric Methods Brain Syst.* **27**, 179–220 (1995).
37. C. P. Ford, The role of D2-autoreceptors in regulating dopamine neuron activity and transmission. *Neuroscience* **282**, 13–22 (2014).
38. P. F. Marcott, S. Gong, P. Donthamsetti, S. G. Grinnell, M. N. Nelson, A. H. Newman, L. Birnbaumer, K. A. Martemyanov, J. A. Javitch, C. P. Ford, Regional heterogeneity of D2-receptor signaling in the dorsal striatum and nucleus accumbens. *Neuron* **98**, 575–587.e4 (2018).
39. A. Usiello, J.-H. Baik, F. Rougé-Pont, R. Picetti, A. Dierich, M. LeMeur, P. V. Piazza, E. Borrelli, Distinct functions of the two isoforms of dopamine D2 receptors. *Nature* **408**, 199–203 (2000).

40. F. Rougé-Pont, A. Usiello, M. Benoit-Marand, F. Gonon, P. V. Piazza, E. Borrelli, Changes in extracellular dopamine induced by morphine and cocaine: Crucial control by D2 receptors. *J. Neurosci.* **22**, 3293–3301 (2002).
41. F. Sun, J. Zeng, M. Jing, J. Zhou, J. Feng, S. F. Owen, Y. Luo, F. Li, H. Wang, T. Yamaguchi, Z. Yong, Y. Gao, W. Peng, L. Wang, S. Zhang, J. Du, D. Lin, M. Xu, A. C. Kreitzer, G. Cui, Y. Li, A genetically encoded fluorescent sensor enables rapid and specific detection of dopamine in flies, fish, and mice. *Cell* **174**, 481–496.e19 (2018).
42. T. Patriarchi, J. R. Cho, K. Merten, M. W. Howe, A. Marley, W.-H. Xiong, R. W. Folk, G. J. Broussard, R. Liang, M. J. Jang, H. Zhong, D. Dombeck, M. von Zastrow, A. Nimmerjahn, V. Gradinaru, J. T. Williams, L. Tian, Ultrafast neuronal imaging of dopamine dynamics with designed genetically encoded sensors. *Science* **360**, eaat4422 (2018).
43. D. B. Pereira, Y. Schmitz, J. Mészáros, P. Merchant, G. Hu, S. Li, A. Henke, J. E. Lizardi-Ortiz, R. J. Karpowicz Jr., T. J. Morgenstern, M. S. Sonders, E. Kanter, P. C. Rodriguez, E. V. Mosharov, D. Sames, D. Sulzer, Fluorescent false neurotransmitter reveals functionally silent dopamine vesicle clusters in the striatum. *Nat. Neurosci.* **19**, 578–586 (2016).
44. C. Liu, L. Kershberg, J. Wang, S. Schneeberger, P. S. Kaeser, Dopamine secretion is mediated by sparse active zone-like release sites. *Cell* **172**, 706–718.e15 (2018).
45. A. Mohebi, J. Pettibone, A. Hamid, J.-M. Wong, R. Kennedy, J. Berke, Forebrain dopamine value signals arise independently from midbrain dopamine cell firing. *Nature* **570**, 65–70 (2019).
46. D. A. Heller, E. S. Jeng, T.-K. Yeung, B. M. Martinez, A. E. Moll, J. B. Gastala, M. S. Strano, Optical detection of DNA conformational polymorphism on single-walled carbon nanotubes. *Science* **311**, 508–511 (2006).
47. L. Cognet, D. A. Tsyboulski, J.-D. R. Rocha, C. D. Doyle, J. M. Tour, R. B. Weisman, Stepwise quenching of exciton fluorescence in carbon nanotubes by single-molecule reactions. *Science* **316**, 1465–1468 (2007).
48. D. Roxbury, P. V. Jena, R. M. Williams, B. Enyedi, P. Niethammer, S. Marcet, M. Verhaegen, S. Blais-Ouellette, D. A. Heller, Hyperspectral microscopy of near-infrared fluorescence enables 17-chirality carbon nanotube imaging. *Sci. Rep.* **5**, 14167 (2015).
49. J. P. Giraldo, M. P. Landry, S.-Y. Kwak, R. M. Jain, M. H. Wong, N. M. Iverson, M. Ben-Naim, M. S. Strano, A ratiometric sensor using single chirality near-infrared fluorescent carbon nanotubes: Application to in vivo monitoring. *Small* **11**, 3973–3984 (2015).
50. J. T. D. Bonis-O'Donnell, R. H. Page, A. G. Beyene, E. G. Tindall, I. R. McFarlane, M. P. Landry, Dual near-infrared two-photon microscopy for deep-tissue dopamine nanosensor imaging. *Adv. Funct. Mater.* **27**, 1702112 (2017).
51. J. B. Ding, K. T. Takasaki, B. L. Sabatini, Supraresolution imaging in brain slices using stimulated-emission depletion two-photon laser scanning microscopy. *Neuron* **63**, 429–437 (2009).
52. F. Wang, G. Dukovic, L. E. Brus, T. F. Heinz, The optical resonances in carbon nanotubes arise from excitons. *Science* **308**, 838–841 (2005).
53. A. D. Edelstein, M. A. Tsuchida, N. Amodaj, H. Pinkard, R. D. Vale, N. Stuurman, Advanced methods of microscope control using μManager software. *J. Biol. Methods* **1**, 10 (2014).
54. A. Vandenberg, D. J. Piekarski, N. Caporale, F. J. Munoz-Cuevas, L. Wilbrecht, Adolescent maturation of inhibitory inputs onto cingulate cortex neurons is cell-type specific and TrkB dependent. *Front. Neural Circuits* **9**, 5 (2015).

**Acknowledgments:** We thank M. Feller, H. Bateup, D. Sulzer, and D. Schaffer for helpful discussions and comments on the manuscript and N. Ouassil for manuscript feedback. **Funding:** We acknowledge support of the NIH NIDA CEBRA Award no. R21DA044010 to L.W. and M.P.L. and the Burroughs Wellcome Fund Career Award at the Scientific Interface (CASI), the Simons Foundation, the Stanley Fahn PDF Junior Faculty Grant with award no. PF-JFA-1760, the Beckman Foundation Young Investigator Award, and the DARPA Young Investigator Award to M.P.L. M.P.L. is a Chan Zuckerberg Biohub investigator. A.G.B. was supported by the NSF Graduate Research Fellowship and an NIH DSPAN F99/K00 grant from NINDS and is an HHMI Gilliam Fellow. **Author contributions:** M.P.L. conceived the project with input from A.G.B. and L.W. A.G.B., K.D., M.P.L., and L.W. designed the studies and wrote the manuscript. A.G.B. performed most of the imaging experiments and the data analysis, and J.T.D.B.-O. automated the data analysis. K.D. performed whole-cell slice electrophysiological recordings. K.D., W.C.L., A.W.T., S.J.Y., D.J.P., and D.Y. performed the surgeries and assisted with the slice generation, control experiments, and nanosensor validation. P.K. performed the FSCV experiments. G.S.P. performed the *M. spicilegus* experiments. All authors edited and commented on the manuscript and gave their approval of the final version. **Competing interests:** M.L., L.W., J.T.D.B.-O., and A.G.B. are authors on a patent application pending with the Regents of the University of California (no. 16/373,542, published 12 April 2018). All other authors declare that they have no competing interests. **Data and materials availability:** All data needed to evaluate the conclusions in the paper are present in the paper and/or the Supplementary Materials. Additional data related to this paper may be requested from the authors. Custom processing software is available on GitHub (https://github.com/jtdbod/Nanosensor-Brain-Imaging).

Submitted 7 December 2018
Accepted 5 June 2019
Published 10 July 2019
10.1126/sciadv.aaw3108

**Citation:** A. G. Beyene, K. Delevich, J. T. Del Bonis-O'Donnell, D. J. Piekarski, W. C. Lin, A. W. Thomas, S. J. Yang, P. Kosillo, D. Yang, G. S. Prounis, L. Wilbrecht, M. P. Landry, Imaging striatal dopamine release using a nongenetically encoded near infrared fluorescent catecholamine nanosensor. *Sci. Adv.* **5**, eaaw3108 (2019).

Science Advances

# Imaging striatal dopamine release using a nongenetically encoded near infrared fluorescent catecholamine nanosensor

Abraham G. Beyene, Kristen Delevich, Jackson Travis Del Bonis-O'Donnell, David J. Piekarski, Wan Chen Lin, A. Wren Thomas, Sarah J. Yang, Polina Kosillo, Darwin Yang, George S. Prounis, Linda Wilbrecht and Markita P. Landry

*Sci Adv* **5** (7), eaaw3108.
DOI: 10.1126/sciadv.aaw3108

---

*Science Advances* (ISSN 2375-2548) is published by the American Association for the Advancement of Science, 1200 New York Avenue NW, Washington, DC 20005.

# Appendix II

US 20190224342A1

(19) **United States**

(12) **Patent Application Publication**

**Landry et al.**

(10) **Pub. No.: US 2019/0224342 A1**

(43) **Pub. Date: Jul. 25, 2019**

(54) **IMAGING NEUROTRANSMITTERS IN VIVO USING FUNCTIONALIZED CARBON NANOTUBES**

(71) Applicant: **The Regents of the University of California**, Oakland, CA (US)

(72) Inventors: **Markita P. Del Carpio Landry**, Berkeley, CA (US); **Linda A. Wilbrecht**, Berkeley, CA (US); **Jackson Travis Del Bonis-O'Donnell**, Berkeley, CA (US); **Abraham G. Beyene**, Berkeley, CA (US)

(73) Assignee: **The Regents of the University of California**, Oakland, CA (US)

(21) Appl. No.: **16/373,542**

(22) Filed: **Apr. 2, 2019**

**Related U.S. Application Data**

(63) Continuation of application No. PCT/US17/55995, filed on Oct. 10, 2017.

(60) Provisional application No. 62/405,963, filed on Oct. 9, 2016.

**Publication Classification**

(51) **Int. Cl.**

| | |
|---|---|
| ***A61K 49/00*** | (2006.01) |
| ***G01N 33/94*** | (2006.01) |
| ***B82Y 5/00*** | (2006.01) |
| ***B82Y 15/00*** | (2006.01) |

(52) **U.S. Cl.**

CPC ..... ***A61K 49/0054*** (2013.01); ***G01N 33/9406*** (2013.01); ***B82Y 5/00*** (2013.01); *Y10S 977/927* (2013.01); *Y10S 977/75* (2013.01); *Y10S 977/92* (2013.01); ***B82Y 15/00*** (2013.01)

(57) **ABSTRACT**

Imaging based detection of changes in extracellular neurotransmitter concentration in living tissue is achieved using novel nanotube-based sensors. The sensors are functionalized, neurocompatible single-walled carbon nanotubes (SWNT) comprising an adsorbed neurotransmitter analyte selective polynucleotide.

# IMAGING NEUROTRANSMITTERS IN VIVO USING FUNCTIONALIZED CARBON NANOTUBES

## INTRODUCTION

**[0001]** Neurotransmitters play a central role in complex neural networks by serving as chemical units of neuronal communication. As a result, spatiotemporal neurotransmitter sensing has the potential to profoundly impact on our understanding of how the brain works, and presents a new platform by which to validate the function of neurological drugs. Therapeutic drugs that target neurotransmitter release are used ubiquitously to treat a vast array of brain and behavioral disorders: for over 60 years, drugs that alter, mimic, or block dopamine have formed the core arsenal for the treatment of neurological disorders such as depression, addiction, schizophrenia, anxiety, Parkinson's disease, and social autism spectrum disorder. However, currently in neuroscience, few analytical methods exist that can detect neurotransmitters with high spatial and temporal resolution in vivo in extracellular space. The difficulty of in vivo analyte detection emanates from the optical density of the brain, and its chemical complexity: Brain tissue scatters most wavelengths of light currently used to perform biological imaging, and neuronal tissue has an abundance of biomolecules that are chemically or structurally similar to the neurotransmitters we wish to detect. Furthermore, neurologically relevant processes occur at technically challenging size (nano) and time (millisecond) scales. Current tools to detect neurotransmitters have shortcomings in five broad areas that are addressed by our technology. (i) electrochemical-based tools don't have the selectivity to differentiate between molecules of similar redox potentials, (ii) electrochemical-based tools don't have appreciable spatial resolution (limited to millimeters), (iii) electrochemical tools can scar tissue limiting use, (iv) fluorescence-based tools don't have appreciable ability to report changes in extracellular concentration, and (v) and fluorescence based tools can photobleach, and may have limited use (due to load re-load requirements in case of fluorescent false neurotransmitters). Relevant literature: Kruss et al., J. Am. Chem. Soc. 2014, 136, 713-724; Tu et al., Nature 460, 250-253 (9 Jul. 2009)

## SUMMARY OF THE INVENTION

**[0002]** We disclose an optical molecular recognition platform that utilizes polymer conjugated carbon nanotubes for the detection of neurotransmitters for use in biological samples in vitro and in vivo, including a physiological fluid like saliva or cerebral spinal fluid, as well as brain tissue, including intact brain and brain portions, such as slices . We disclose the use of polymer-functionalized carbon nanotubes for in vivo molecular detection of neurotransmitter analytes, and we exemplify our invention using the detection of neurotransmitters in a live slice of brain tissue. Our invention uses the optical properties of polymer-functionalized carbon nanotubes to detect the analyte. Detection of neurotransmitters is accomplished both in space and time, reversibly. Our sensors are biocompatiable and neurocompatible, and allow optical imaging of neurotransmitter spatial distribution, concentration, and dynamics in real time and in living tissue. The invention takes advantage of favorable fluorescence properties of carbon nanotubes, such as carbon nanotube emission in the near infrared (a region of relative optical tissue transparency), and non-photobleaching fluorescence. The near infrared emission is minimally scattered in biological systems, enabling their use in deep tissues. The non-photobleaching fluorescence of our neurotransmitter sensors enable their use in hours-long experiments. Infrared emission and non-photobleaching fluorescence benefits are features that are lacking in modern fluorescence imaging methods.

**[0003]** In embodiments, the invention provides;

**[0004]** measurement of neurotransmitter levels or dynamics in neurotransmitter concentrations using optical imaging in tissue or fluid; these measurements may be performed in the brain or peripheral nervous system of anesthetized or awake animal subjects, or in reduced brain preparations (e.g. brain slices of any species);

**[0005]** dynamic spatial and temporal readout of neurotransmitter concentrations in any part of the brain or peripheral nervous system. It may also be applied to measure and image neurotransmitter concentrations in tissue or fluid samples that may contain neurotransmitters;

**[0006]** monitoring neurotransmitter levels in biological solutions or preparations; for example in saliva or cerebrospinal fluid;

**[0007]** brain imaging for use in various settings such as diagnostics in health care facilities, teaching, and research in academic settings;

**[0008]** methods and compositions to quantitatively evaluate and or validate the mechanism of action and/or efficacy of new and or established drugs or other therapeutics that target neurotransmission. Examples of such drugs include Levodopa and dopamine antagonists (e.g. Ropinirole, Pramipexole, Loxapine, Thioridazine, Thiothixene, Trifluperidol), agonists (e.g. Modafinil, Rotigotine, Dizocilpine, Ciladopa, Fenoldopam, Rotigotine, Memantine), reuptake inhibitors (e.g. Desoxypipradrol, Troparil, Benztropine, Mesocarb, Mazindol, Altropane), and releasing agents (e.g. Phenmetrazine, Mefenorex, Amfecloral, Fenproporex). Neurotransmitter measurements may be achieved in either blood, saliva, CSF, brain tissue, brain slices, and or anesthetized or awake and behaving animals;

**[0009]** monitoring progression of brain diseases;

**[0010]** methods and compositions for identifying parts of the brain that have suffered trauma (i.e. traumatic brain injury) and can be used to determine if (and to what extent) that injury site has affected its ability to undergo normal neurotransmission behavior;

**[0011]** methods and compositions to determine how external stimuli (perceptual, social, chemical etc.) affect neurotransmission in the brain of awake and behaving animals;

**[0012]** functionalized, neurocompatible single-walled carbon nanotubes (SWNT) and their use for imaging of neurotransmitters in vivo, in live animals; and/or

**[0013]** sensors configured to image complex neural physiology by monitoring the spatial and temporal dynamics of neurotransmitters in live brain tissue.

**[0014]** In an aspect the invention provides a functionalized, neurocompatible single-walled carbon nanotube (SWNT) comprising an adsorbed neurotransmitter analyte selective polynucleotide covalently bound to a neurocompatible polyethyleneglycol (PEG).

**[0015]** In embodiments:

**[0016]** the polynucleotide is ssDNA or ssRNA;

**[0017]** the polynucleotide has a periodic purine-pyrimidine pattern, or any combination of purine and pyrimidine bases;

**[0018]** the polynucleotide is polyGT is (GT)n, wherein n is an integer 2-500, or 3-150, or 4-30, or about 15;

**[0019]** the analyte is a neurotransmitter selected from a catecholamine (e.g. epinephrine (adrenaline), norepinephrine (noradrenaline), and dopamine), histamine, 5-hydroxytryptamine (serotonin), γ-aminobutyric acid (GABA), glutamine, glutamic acid or a neurotransmitter metabolite selected from L-3,4-dihydroxyphenylalanine (L-dopa), 3,4-Dihydroxyphenylacetic acid (DOPAC), homovannilic acid and tyramine; and/or

**[0020]** the PEG is PEG MW 200-40000, or 400-20000, or about 5000.

**[0021]** In another aspect the invention provides a functionalized, neurocompatible single-walled carbon nanotube (SWNT) comprising an adsorbed dopamine-selective polynucleotide of sequence $(GT)_6$.

**[0022]** In embodiments:

**[0023]** the polynucleotide is covalently bound to a neurocompatible polyethyleneglycol (PEG); and/or

**[0024]** the PEG is PEG MW 200-40000, or 400-20000, or about 5000.

**[0025]** The invention also provides methods of imaging neurotransmitters in vivo using functionalized, neurocompatible nanotube sensors, particularly wherein the sensors are delivered to the brain of a live mammal, such as wherein the changes in extracellular neurotransmitter concentration are detected in neural tissue, cerebrospinal fluid, blood or saliva, and particularly wherein the changes are detected in neural tissue.

**[0026]** The invention encompasses all combination of the particular embodiments recited herein, as if each combination had been laboriously recited.

## DESCRIPTION OF PARTICULAR EMBODIMENTS OF THE INVENTION

**[0027]** Unless contraindicated or noted otherwise, in these descriptions and throughout this specification, the terms “a” and “an” mean one or more, the term “or” means and/or and polynucleotide sequences are understood to encompass opposite strands as well as alternative backbones described herein.

**[0028]** It is understood that the examples and embodiments described herein are for illustrative purposes only and that various modifications or changes in light thereof will be suggested to persons skilled in the art and are to be included within the spirit and purview of this application and scope of the appended claims. All publications, patents, and patent applications cited herein, including citations therein, are hereby incorporated by reference in their entirety for all purposes.

**[0029]** We disclose an optical molecular recognition platform that utilizes polymer conjugated carbon nanotubes for the detection of neurotransmitters for use in vivo. When a polymer is non-covalently conjugated to the surface of a single-walled carbon nanotube (SWCNT), a corona phase forms with unique molecular recognition sites for specific biomolecules (in this case, neurotransmitters). When an analyte binds to the polymer-nanotube conjugate, the corona phase is perturbed, changing the optical properties of the nanoparticle. This modulation in the fluorescent emission of the nanoparticle is reversible, and serves as the recognition signal for the analyte. This fluorescence modulation, when measured using fluorescence microscopy, provides a readout of neurotransmitter concentration with spatial and temporal resolution for in vivo experiments. Our method holds distinct advantages over other optical methods because of the near infrared emissivity of carbon nanotubes where scattering by biological tissue is minimal.

**[0030]** Adding to the advantages of our platform is the optical stability of carbon nanotubes that allow extended imaging with no loss of fluorescence output, a property critical for performing long-term imaging experiments that have yet to be implemented with other fluorescent probes. Our sensors convey information on neurotransmitter concentration on size and time scales that few other tools in neuroscience provide. The selectivity of the sensors for a particular neurotransmitter ensures that the signal transduced is that of a particular neurotransmitter. Some of the general utilities for our invention are:

**[0031]** Detection of neurotransmitter release in viable neural tissue (in vivo);

**[0032]** Conveying neurotransmitter concentration information on spatial and temporal scales appropriate to study physiological processes in live brain tissue;

**[0033]** Probing complex neural circuitry by monitoring changes in neurotransmitter concentration in different parts of the brain in real time;

**[0034]** Probing how neural plasticity is affected (or affects) neurotransmitter release;

**[0035]** Examining effect of pharmaceutical drugs on brain function as conveyed by changes in neurotransmitter concentration;

**[0036]** Monitoring changes in neurotransmitter concentration during behavior studies involving awake and behaving animals;

**[0037]** Monitoring changes in physiology (function) caused by pharmaceutical agents, brain disorders or traumatic injuries; and/or

**[0038]** Imaging brain activity for diagnostic or therapeutic purposes.

**[0039]** Our SWCNT nanosensors are neurocompatible, emit in the near-infrared spectrum and offer a new optical method for detection of neurotransmitters. The optical methods enable greater spatial resolution and chronic recording. In combination with other imaging methods can provide a wealth of new information about release and diffusion, the action of drugs with abuse potential or therapeutic application.

**[0040]** Our invention enables non-invasively imaging dynamic neuronal activity across large swaths of the brain, making it uniquely suited to enabling neurotransmitter imaging in real-time in awake and behaving animals; for example, the invention may be used to validate drugs (antipsychotics, antidepressants, stimulants, etc) that target neurotransmission. The invention provides imaging brain circuitry on spatiotemporal scales appropriate for neuroscience and for drug validation.

**[0041]** Competing methods include (1) Fast scan cyclic voltometry and amperometry (FSCV), (2) CNiFERs, and (3) fluorescent false neurotransmitters (FFNs). FSCV and amperometry are electrode-based methods that use oxidation of catecholamines at a carbon fiber to report catecholamine levels. CNiFER is cell-based and is based on slow G protein-coupled receptor responses. FSCV and CNiFER methods have low spatial resolution and recording sites are placed blind to axon site. These methods have not been sufficient to enable continuous and spatially and temporally-relevant measurements of dopamine and other modulatory neurotransmitters in the neocortex. Fluorescent false neurotransmitters (FFNs) can be used to study dopamine release but are not easily loaded and reloaded for long term use. FFNs do not report neurotransmitter levels in extracellular space. Calcium imaging can show bouton activity preceding release but may not report longer term release and do not report neurotransmitter levels in extra cellular space.

**[0042]** Advantages of our sensors in contrast to FSCV include: Cyclic voltammetry provides little in the way of spatial resolution of analytes it measures. Cyclic voltammetry probes measure millimeters at best, and must be inserted directly into brain tissue to acquire a reading. Positioning next to release sites is not feasible when they are sparse. In contrast, our nanosensors are nanometers in size (1×200 nm) and can be injected directly into brain tissue in a relatively non-invasive manner Compatible imaging methods can be used to determine distance from release sites and enables detection with high spatial resolution for comparing brain regions or for following diffusion from a site. The nanometer-scale size of our sensors enables us to report on nanometer-scale spatial changes in neurotransmitter concentration, which is relevant to the size of the synaptic cleft (300 ±150 nm) in which neurotransmission occurs between neuronal cells. (ii) FSCV has low selectivity for a neurotransmitter target of interest: if analytes with similar redox potentials exist within the region of interest, this signal will confound the signal from dopamine release. Cyclic voltammetry readings will report on the presence of any molecules with a similar redox potential to the target neurotransmitter. In contrast, our nanosensors are selective for a neurotransmitter of interest. (iii) Cost and user-friendliness. Compared to our nanosensors, FSCV is expensive, requires high degree of expertise to operate, and is invasive. (iv) FSCV and comparable methods are susceptible to probe fouling, such that each subsequent reading may exhibit hysteresis that is a function of electrode fouling. In contrast, our sensors have a nanosecond residence time on the nanosensors surface (as determined by molecular dynamics simulations), suggesting that there is no fouling of our sensors by chelation of biomolecules on the sensor surface. Our data show several iterations of dopamine detection in an acute brain tissue slice, exemplifying the non-fouling nature of our sensors.

**[0043]** Advantages of our sensors in contrast to fluorescence based techniques include (i) infinite fluorescence lifetimes (no photobleaching) enabling—for the first time—measurement of neurotransmitters for hours-long timescales in artificial cerebrospinal fluid (aCSF). (ii) Our nanosensors are reversible. CNiFER can only report on the cumulative GPCR activity. FFNs only report on neurotransmitter release. Our sensors can directly report both the appearance but also the disappearance of neurotransmitters in extracellular space. This enables us to measure both neurotransmitter release and neurotransmitter re-uptake, both of which are key elements of modulatory neurotransmission. In areas of sparse release, we may also be able to visualize diffusion from a release site, which would also add new ability. (iii) Our nanosensors are nano-scale. CNiFER are the size of HEK293 cells that encode their signal (10-15 μm). Therefore, CNiFER are inherently more 'invasive' when inserted into brain tissue, as they require a larger accommodation volume. Additionally, CNiFER can only report on indirect GPCR activity within a spatial limit of detection that matches their size (tens of microns). Conversely, our sensors are nanometers in size (1 nm×200 nm) and can be used to report on nanometer-scale spatial changes in neurotransmitter concentration, which is relevant to the size of the synaptic cleft (300±150 nm) in which neurotransmission occurs between neuronal cells. (iv) CNiFER cells respond on the timescale of seconds to minutes, whereas our sensors respond on millisecond timescales. In other words, from the time when a neurotransmitter is released until the sensor responds to its presence, CNiFER cells will have a second to minute-long time lag. Our sensor's millisecond temporal responsivity matches the time-scale upon which neurotransmitters are released in the brain. (v) Our sensor signals can penetrate tissue and bone with a near-infrared signal. Unlike other fluorescent methods, we can acquire fluorescence signal with less scatter from our sensor through brain tissue and through bone (cranium) tissue. We demonstrate the bone-penetrating capabilities, in which we have placed our sensors on top of a mouse cranium, and monitor the fluorescence of these nanosensors upon addition of neurotransmitter. We can detect a clear increase in fluorescence upon addition of neurotransmitter through the mouse cranium.

**[0044]** A significant utility of our invention lies in its ability to help probe complex neural physiology by monitoring the spatial and temporal dynamics of neurotransmitters in live brain tissue; for example, the effects of pharmaceutical therapies on brain function can be studied in real time.

**[0045]** In an aspect the invention provides a functionalized, neurocompatible single-walled carbon nanotube (SWNT) comprising an adsorbed neurotransmitter analyte selective polynucleotide covalently bound to a neurocompatible polyethyleneglycol (PEG).

**[0046]** SWNTs comprising an adsorbed neurotransmitter analyte selective polynucleotide are known in the art, and the methods of making and criteria for selecting analyte selective polynucleotides are established. Suitable polynucleotide are typically, ssDNA or ssRNA, which may be present in a variety of structural conformations. Preferred polynucleotides have a periodic purine-pyrimidine pattern, such as polyGT is (GT)n, wherein n is an integer, such as 2-500, or 3-150, or 4-30, or in a particular example, about 15.

**[0047]** We have validated the disclosed methods with a variety of neurotransmitter analytes, including catecholamines, histamine, 5-hydroxytryptamine (serotonin), γ-aminobutyric acid (GABA), glutamine, glutamic acid, L-3,4-dihydroxyphenylalanine (L-dopa), 3,4-Dihydroxyphenylacetic acid (DOPAC), homovannilic acid and tyramine.

**[0048]** Suitable neurocompatible polyethyleneglycol (PEG) components are readily determined empirically, confirmed by lack of effective toxicity, as exemplified below, and include a variety of structures (e.g. branching) and molecular weight, including PEG MW 200-40000, or 400-20000, or about 5000.

**[0049]** To demonstrate our nanosensor's utility in living brain tissue, we detail experiments herein in which the release of endogenous neurotransmitter is monitored from acute brain slices stimulated by high potassium ($K^+$) containing buffer solution. We describe the synthesis of the sensors, detail the preparation of brain slices embedded with our neurotransmittersensors, and provide experimental details for the imaging of brain slices embedded with our nanosensors.

## EXAMPLES

### 1. Imaging Dopamine in Brain Tissue Using Synthetic Infrared Nanosensors

**[0050]** The optical nanosensors are synthesized by suspending single walled carbon nanotubes in pegylated $(GT)_{15}$ DNA by probe tip sonication in a 100 mM NaCl buffer solution. The pegylation of the DNA strand can be achieved by reacting maleimide end-modified polyethylene glycol (PEG, 3 kDa) with a 5' thiolated $(GT)_{15}$ DNA. The pegylated DNA is then sonicated for 10 minutes at ~5 W power setting. Finally, the sonicated mixture is centrifuged to remove unsuspended nanotubes, and the recovered supernatant characterized using a UV-Vis spectrometer. This simple and easily scalable process gives a stable sensor suspension that can be stored at room temperature for extended time periods. The user can dilute the suspensions to desired nanotube concentrations for in vivo and in vitro use.

**[0051]** Acute brain slices are prepared from anesthetized mice. The brain is quickly extracted from the skull and mounted on a vibratome for slicing. The vibratome was pre-chilled to 4° C. and the sample tray filled with $O_2$ saturated aCSF buffer. At all times, the brain and recovered brain slices were kept in continuously gassed (95% $O_2$, 5% $CO_2$) aCSF buffer at 4° C. Sensors were diluted to a nanotube concentration of 25 mg/L in PBS (phosphate buffered saline) before being injected into the brain. Approximately 20 μL of sensor volume was injected into the mounted brain using Hamilton Neuros Syringes, from which 300 μm slices were recovered. After recovery of 3 such slices, an additional 20 μL of sensor was injected into the brain, after which brain slices continued to be recovered. 20 μL sensor volume was injected for every 3 slices recovered from the brain until enough brain slices were recovered for the experiment. Each 20 μL volume injection was delivered into three to five distinct regions to enable neurotransmitter detection in various regions of the brain.

**[0052]** Sensors are delivered into the brain via injection. The injection site and its periphery will house a bolus of sensors, which detect neurotransmitter molecules and changes in neurotransmitter concentration as neurotransmitter diffuses out of their point of release. Owing to their small size, some of our sensors may be inside the synaptic region (interface between two neuronal axons where neurotransmitter release takes place); however, a significant portion of the injected sensors will be extrasynaptic in location. Regardless of their location, diffusion of neurotransmitters is the primary mechanism by which neurotransmitters signal between cells. Once in contact with extracellular sensors, neurotransmitter molecules (or other specific sensor analytes) cause conformational changes of the pegylated $(GT)_{15}$ DNA on the surface of the nanotube, resulting in modulation of fluorescence behavior; in the case of neurotransmitter detection, the modulation produces a rapid increase in the fluorescence of the carbon nanotubes.

**[0053]** The depolarization wave that triggers release of neurotransmitter can be elicited using electrical, chemical, or optical stimulation. For our demonstration, we use chemical stimulation using a high 15-35 mM potassium ($K^+$) aCSF buffer. The high concentration of potassium causes an ion imbalance between the cytoplasmic and extracellular environment, which causes neuronal membrane depolarization and neurotransmiter release.

**[0054]** We imaged direct nanosensor-based neurotransmitter release in brain tissue in four acute slices, and representative intensity-time traces. When neurotransmitter is released from neurons, the near-infrared fluorescence intensity of our sensors increases. The increase in intensity is normalized and presented as a plot against time in four different brain slices. Our results show the near-infrared fluorescence spectra of our sensors, and the characteristic multi-peak emission of our sensor emission profile. This spectrum serves to confirm that the sensor intensity increase imaged in the brain tissue slice is caused by modulations in the fluorescent properties of the nanotubes (as a result of neurotransmitter release), and not an artifact caused by changes in baseline tissue fluorescence.

**[0055]** We also tested the reversibility of our sensors in living neural tissue. Reversibility demonstrates that once neurotransmitter causes conformational changes that increase fluorescence intensity of our sensors, the subsequent removal of neurotransmitter from the extracellular space can reverse the fluorescence intensity increase, in effect resetting our sensors for detection of subsequent neurotransmitter release events. Sensor reversibility is vital to monitoring dynamic neurotransmitter concentrations, and a feature lacking in many existing technologies for neurotransmitter detection.

**[0056]** We have confirmed our neurotransmitter nanosensor is functional in ex vivo striatal tissue by using high K+ to drive bulk neurotransmitter release, for multiple stimulation and wash cycles, over the course of 80 minutes. These data also reduce concerns about potential "biofouling" in which the sensor is activated or inactivated by non-specific binding when placed in tissue, or in which the sensor degrades after repeated use or after extended time.

**[0057]** In vitro experiments show the neurotransmitter nanosensors can report neurotransmitter concentrations that range from 100 nM to 0.1 mM, a range relevant to endogenous neurophysiology. At the single sensor level, we can detect picomolar (pM) quantities of neurotransmitter. The through-cranium neurotransmitter detection capabilities we demonstrate, enabled by the tissue and bone-transparency of infrared fluorescence wavelengths emitted by our sensors, indicate our sensors will enable detection of neurotransmitters in an intact brain structure, through the cranium bone.

**[0058]** We have applied our model of sensor response in striatal tissue to the expected pattern of neurotransmitter release as detailed in the literature, for both positive and negative reward prediction error responses. We estimate that neurotransmitter release driven by a shift from tonic firing at 5 Hz to a phasic burst at 20 Hz for 500 msec (a positive reward prediction error) should be induce a deltaF/F of 0.27 using bulk phase detection. Movement from a tonic rate at 5 Hz to 1 Hz pause for 500 msec (a negative reward prediction error) should produce a delta F/F of −0.07. These delta F/F estimates are modest but sufficient and are comparable to levels reported in experiments using genetically encoded calcium indicators such as GCAMP for functional imaging in rodents. These estimates indicate that this sensor is a useful tool for detection of changes in modulatory neurotransmitter levels relevant to behavioral studies in awake behaving animals.

**[0059]** We have tested and confirmed imaging of a panel of neurotransmitter analytes, including epinephrine (adrenaline), norepinephrine (noradrenaline), dopamine, 5-hydroxytryptamine (serotonin), glutamic acid, L-3,4-dihydroxyphenylalanine (L-dopa), 3,4-Dihydroxyphenylacetic acid (DOPAC), homovannilic acid and tyramine

## 2. Molecular Recognition Mechanisms Revealed in DNA-Wrapped Carbon Nanotubes

**[0060]** In this example we demonstrate molecular recognition mechanisms underlying the SWNT sensing activity. Varying the length of DNA polymers wrapping SWNTs yielded highly selective sensors for molecular analytes dopamine and norepinephrine. Molecular dynamics studies identified that the selectivity in these new sensors originates from DNA polymers that assume circular conformations on SWNTs, and perfectly wrap the SWNT once along its circumference. We identify that DNA conformations create distinct modulations of the electrostatic environment within SWNT, which can lead to enhanced localization of the exciton. We also observe charge transfer to SWNTs in ssDNA-SWNT composites, which can influence exciton relaxation pathway and relaxation rates. Surfactant exchange reveals dopamine molecular recognition mechanism: polynucleotide surface coverage.

**[0061]** To identify the mechanisms that enable selective molecular recognition of dopamine by SWNT-based optical nanosensors, we performed all-atom molecular dynamics (MD) simulations, quantum mechanical (QM) calculations, and fluorescence imaging of the $(GT)_{15}$-SWNT nanosensor selective for neurotransmitter dopamine. MD simulations reveal that polymer length dictates the structure of the polymer on the SWNT, whereby 12 nucleoside-length single-stranded DNA (ssDNA) polymers form rings around SWNT instead of helices. The SWNT surface-adsorbed polymer generates patterns of electrostatic potentials on the SWNT surface and strongly localizes excitons, leading to a prevalence of non-radiative exciton recombination in SWNT. MD and QM calculations identify charge transfer between the polymer wrapping and the SWNT as the mechanism of PL attenuation, which can be reversed in the presence of the neurotransmitter analyte. Quantum mechanical (QM) calculations show that adsorbed nucleosides of the polymer dope the SWNT, forming charge transfer sites along the nanotube axis. In the presence of these doping sites, strongly localized excitons recombine efficiently through a dominant non-radiative multiphonon decay process. This decay is abolished or severely slowed in the presence of dopamine, leading to the brightening of photoluminescence (PL). We validate our calculations with fluorescence spectroscopy and microscopy of SWNT nanosensors, and demonstrate that we can implement our QM and MD strategy to control exciton recombination and analyte selectivity to discover a new fluorescent sensor for neurotransmitter norepinephrine. Our work explores the wide range of time-scales over which fluorescent probes selectively photoluminesce in the presence of neurological targets: charge transfer (femtosecond via QM calculations), selective analyte binding and exciton recombination (nanosecond via MD simulations), and neurotransmitter imaging (millisecond via infrared microscopy).

**[0062]** MD simulations show DNA polymer length modulates helix-to-ring transition on SWNT. Variations in the fluorescence (the PL quantum yield) of SWNTs wrapped by different polymers can depend on the chemical composition of the polymers, interaction types and strengths, and the physical parameters of the SWNT environment, such as the dielectric screening. We implement MD simulations of known SWNT-based dopamine nanosensor $(GT)_{15}$-SWNT to elucidate how the polymer creates patterns in the electrostatic environment of the SWNTs, and to examine how this environment affects SWNT PL. The initial states of ssDNA-SWNT systems were based on reported structures of ssDNA adsorbed to SWNT, which demonstrated that ssDNA polymers wrap SWNTs helically. Our MD simulations show that $(GT)_{15}$ ssDNA remains equilibrated onto the SWNT surface in a helical structure within the 200 ns simulation length, consistent with previous studies, and showed no significant structural deviations from its initial helical conformation.

**[0063]** To examine the electrostatic effect of the ss-$(GT)_{15}$ polymer on SWNT, we calculated the electrostatic potential induced by the ss-$(GT)_{15}$ at the SWNT surface. The calculated potential includes all molecules present in the SWNT environment: the ssDNA polymer, water, and ions, including the $Na^+$ cations adsorbed over long timescales within DNA pockets. We find that ss-$(GT)_{15}$ induces regions of negative and positive electrostatic potential as a 'footprint' under the polymer, which extend ~4 nm in contiguous length, and roughly follow the helical pattern of the ssDNA.

**[0064]** Motivated by the observed electrostatic footprinting of polymers adsorbed to SWNT, we further explored alternate $(GT)_n$ ssDNA polymer-SWNT structures, where n indicates ssDNA polymers containing a varying number of repeating (GT) units. While ssDNA molecules that encapsulate SWNTs several times are observed to adopt helical conformations, shorter ssDNA oligonucleotides adopt different surface adsorbed patterns, which can afford a unique control parameter over electrostatic footprinting and SWNT exciton recombination. In particular, SWNTs that are widely used for fluorescence imaging and sensing have ~1.2 nm diameters, which can accommodate a singly wrapped 12-mer (4.08 nm long) oligonucleotide. Thus, we performed MD simulations of $(GT)_6$ oligonucleotide initially helically equilibrated to the surface of a (9,4) SWNT, to replicate the initial conditions of the simulated $(GT)_{15}$-SWNT system. During a short 20 ns simulation, $(GT)_6$ polymer rearranged from its initial helical conformation to a ring-like structure; such helix-to-ring transitions were reproducibly observed in >5 independent MD simulations. While the system contains a single ssDNA molecule, fluorescent SWNT nanosensors typically contain many ssDNA molecules adsorbed onto a single SWNT. Therefore, to better emulate experimental conditions, we examined multiple ssDNA-$(GT)_6$ polymers wrapping the SWNT. Following simulation, we again observe helix-to-ring transition for all $(GT)_6$ polymers. The DNAs in ring conformations are highly ordered, as evidenced by distinct sharp peaks that appear at approximately equal intervals in the radial distribution function of DNA phosphate groups. Electrostatic footprinting induced by the ring-like structures of $(GT)_6$ polymers on SWNT is observed, following the physical adsorption pattern of the electrostatic potential induced by the $(GT)_6$ polymer. The resulting electrostatic potential map on the SWNT surface appears in distinct ring-like regions of alternating positive and negative potential along the SWNT surface, where each electrostatic pocket measures ~1.5 nm in contiguous length. The negative electrostatic potential pockets are observed primarily beneath guanine nucleotides, while the positive electrostatic potential pockets are observed beneath thymine nucleotides.

**[0065]** Electrostatic footprinting of SWNT by circumference-length $(GT)_N$ polymers yield high turn-on sensors for dopamine and norepinephrine. For in vivo applications of neurotransmitter nanosensors, a strong fluorescence turn-on response is necessary. Prior work shows that the fluorescence intensity of $ss(GT)_{15}$-SWNT increases by as much as 90% upon exposure to 100 μM dopamine At physiological concentrations (~1 μM), the expected ΔF/F is on the order of 30%. Dopamine addition to the $ss(GT)_{15}$-SWNT sensor does not perturb the SWNT absorption cross section, thus the fluorescence intensity increase results from an increase in dopamine-induced SWNT quantum efficiency. Guided by the theoretically predicted electrostatic confinement of SWNT excitons by $(GT)_6$ polymers, we synthesized a $(GT)_N$ based ssDNA polymer library to probe the effects of polymer conformation on nanosensor sensitivity and selectivity to neurotransmitter dopamine We produced a library of $(GT)_N$ ssDNA sequences for N=1, 4, 6, 7, 8, 12, 15, 19, 22, 26, and 30 using a previously-described protocol. All sequences from N=4 to N=30 produced DNA-SWNT suspensions, with the exception of N=1 that did not suspend SWNT. We measured each $(GT)_N$-SWNT sensor's response to 100 μM dopamine Consistent with previous results, dopamine addition increases SWNT fluorescence for all sequences. We observe a surprising length-dependent trend in nanosensor response to 100 μM dopamine, for which the previously reported $(GT)_{15}$-SWNT nanosensor represents an apparent minimum ($\Delta F/F_0$=45%), and $(GT)_6$-SWNT a maximum ($\Delta F/F_0$=3500%). Short $(GT)_N$ repeats (N=4, 6, 7, 8) yield $\Delta F/F_0$=1400%, 2400%, 1700%, and 1000% in response to **100** μM dopamine, respectively, for the (9,4) SWNT chirality. For longer sequences (N=12, 15, 19, 22, 26, 30), we observe corresponding $\Delta F/F_0$=45%, 45%, 50%, 60%, 40%, and 150% in response to 100 μM dopamine, respectively. We identify ssDNA polymers capable of ring-like electrostatic footprinting as having strong turn-on responses to dopamine.

**[0066]** We next examined the baseline fluorescence intensity of equimolar aliquots of each DNA-SWNT suspension in our library, we observe that short (GT) repeat sequences (N=4, 6, 7, 8) exhibit strongly quenched baseline fluorescence, representing 25%, 5%, 15%, and 40% of the baseline fluorescence exhibited by $(GT)_{15}$-SWNT when compared at the (9,4) chirality peak. Conversely, long sequences (N>=12) exhibit approximately the same degree of baseline fluorescence as compared to $(GT)_{15}$-SWNT. In general, the pre-dopamine fluorescence of $(GT)_N$-SWNT suspensions is lower for sequences where N≤8, indicating that polynucleotide sequences exceeding roughly twice the average SWNT circumference in length will adopt a helical SWNT-adsorbed structure, as confirmed by our MD simulations of $(GT)_{15}$-SWNT and $(GT)_6$-SWNT. We thus identify polymer length as a key modulator of SWNT fluorescence quantum yield, which can be exploited for maximizing nanosensor $\Delta F/F_0$ signal. We further identify the $(GT)_6$-SWNT complex as the most suitable nanosensor for imaging dopamine and norepinephrine. DNA-SWNT absorption spectra remain invariant to the addition of dopamine, further indicating that quantum yield increases are what drive the increase in fluorescence for short and long sequences.

**[0067]** To validate the potential in vivo imaging use of $(GT)_6$ SWNT for dopamine and norepinephrine, we developed fluorescence response curves for $(GT)_6$-SWNT suspension by varying concentrations of norepinephrine and dopamine We fit our experimental data using the Hill equation to obtain the dissociation constant for sensor-analyte interaction. We determined the dissociation constants to be 15 μM for norepinephrine and 20 μM for dopamine. Both dopamine and norepinephrine fluorescence turn-on behavior is suitable for measuring neurotransmitter concentrations in biologically-relevant regimes encompassing tonic and phasic firing indicating these sensors are suitable for in vivo imaging of modulatory neurotransmission. A burst of activity from dopaminergic neurons in the striatum can yield local dopamine concentrations on the order of 1 μM to 5 μM. The strong turn-on response of $ss(GT)_6$-SWNT nanosensors is crucial for studying the slow tonic firing of dopaminergic neurons where extracellular dopamine concentrations vary transiently from 10 nM to 100 nM. Under such neuronal activity, only $(GT)_6$-SWNT sensors produce a strong $\Delta F/F_0$ signal to enable in vivo use, and discriminate between transience in tonic firing. We note that compared to the previously reported $ss(GT)_{15}$ based dopamine sensor, the dopamine-induced fluorescence response from our $ss(GT)_6$ sensor is nearly an order of magnitude higher, and significantly more selective toward dopamine and norepinephrine, showing nearly no cross-responsivity for other neurologically-relevant analytes in our screening library. We owe this increased selectivity to the molecular modes of interaction between the catecholamine and nucleosides on the DNA polymer of $ss(GT)_6$-SWNT, as we describe below. Control experiments with $(C)_{30}$-SWNT and $(C)_{12}$-SWNT show these DNA-SWNT conjugates are nonresponsive when exposed to either dopamine or norepinephrine, attributing the selectivity of our nanosensors to the (GT) base sequence, and the sensitivity to the polymer length and subsequent SWNT electrostatic footprinting.

**[0068]** Polymer length modulates stability of polymer on SWNT. We examined the stability of all $(GT)_N$-SWNT suspensions using fluorescence and absorbance spectroscopy. To rule out the possibility that spontaneous DNA polymer rearrangement contributes to the large increase in nanosensor fluorescence after addition of dopamine, we measured the time-dependent fluorescence of all $(GT)_N$-SWNT suspensions using fluorescence spectroscopy. Prior work shows that DNA-SWNT fluorescence stability directly correlates with DNA polymer stability on the SWNT. To test stability using fluorescence, we diluted all $(GT)_N$-SWNT suspensions to equimolar SWNT concentrations and measured their fluorescence spectra over the course of 140 minutes immediately following dilution. Most of the $(GT)_N$-SWCNT suspensions we examined exhibited stable fluorescence (<−15% change) with the exception of $(GT)_4$-SWNT, which showed a final −40% modulation in fluorescence. For all $(GT)_N$-SWNT suspensions, the time-dependent fluorescence modulations were negative, compared to the increase in fluorescence induced by dopamine, further confirming that increase in fluorescence observed immediately after addition of dopamine is due to the dopamine analyte, and unlikely to have been caused by volume perturbations or spontaneous polymer rearrangement on the surface of the carbon nanotube. The differences in fluorescence modulation experienced by each suspension indicate that polymer length affects the base stacking stability of the

$(GT)_N$-SWNT suspensions with an apparent instability for N≤4. Absorbance measurements support the trend observed from fluorescence measurements. Absorbance measurement of the as-made $(GT)_N$-SWNT suspension exhibits strong absorption at ~260 nm, suggesting excess, unadsorbed DNA in solution. The absorbance peak at 260 nm is abolished by removing unsuspended polymer by filter centrifugation. Absorbance measurements at the DNA absorbance peak reveal that no ssDNA polymer desorption occurs from any $(GT)_N$-SWNT sample, with the exception of $(GT)_4$-SWNT that shows appreciable $(GT)_4$ polymer desorption from SWNT after one week at room temperature. Our results indicate that $(GT)_N$ sequences with N>4 form stable non-covalent conjugates with SWNT and that SWNT PL modulation observed in the presence of dopamine results from the polymer-mediated modulation in SWNT quantum yield.

**[0069]** Surfactant exchange reveals dopamine molecular recognition mechanism: dopamine-binding pockets from polymer surface coverage. We measured the relative surface coverage of SWNT by $(GT)_N$ polymers in our library with surfactant exchange experiments. When added ssDNA-SWNT, surfactant sodium cholate (SC) adsorbs to exposed SWNT surface, and can also displace weakly adsorbed DNA regions, causing a solvatochromic SWNT fluorescence peak shift, as reported previously. Addition of 1 wt % SC to $(GT)_N$-SWNT induces solvatochromic shifts in SWNT fluorescence peaks, with the largest solvatochromic observed for $(GT)_4$-SWNT, further indicating $(GT)_4$ is the least stably adsorbed sequence on the SWNT. Sequences above N=4 (N=6 to N=30) all showed minimal SC-induced solvatochromic shifting, indicating that for polymer lengths >4, polynucleotide polymers remain stably bound to the SWNT. We repeated SC solvatochromic shift experiments for all $(GT)_N$-SWNT suspensions pre-incubated in 100 μM dopamine Surprisingly, addition of dopamine to $(GT)_N$-SWNT suspensions pre-incubated with dopamine either reduces or eliminates the SC-induced solvatochromic shifting. As such, it appears that dopamine stabilizes polymer adsorption onto the SWNT surface, even for polymers such as N=4 previously identified to be unstably bound. We disclose that dopamine stabilization of $(GT)_N$ polymers on SWNT arises from a selective interaction between dopamine and $(GT)_N$-SWNT, and further, that dopamine trapped in these $(GT)_N$ polymer binding pockets enhance PL by direct interaction with the adsorbed polymer and the SWNT, and as a result of these interactions, the PL quantum yield of SWNT sensors is selectively enhanced by polymer-induced trapping of dopamine.

**[0070]** Adsorbed Dopamine Modulates ssDNA Conformation and Electrostatic Potential at SWNT. To further examine the molecular recognition mechanism of dopamine by $(GT)_N$-SWNT nanosensors, we performed all-atom MD simulations of ssDNA-$(GT)_{15}$ and ssDNA-$(GT)_6$-SWNT in the presence of dopamine. Several independent MD simulations revealed that dopamine can influence ssDNA conformations and that dopamine has multiple binding poses that are transient.

**[0071]** We prepared representative binding poses of dopamine to ssDNA-$(GT)_{15}$ and ssDNA-$(GT)_6$-SWNTs. Dopamine can insert into SWNT regions that transiently have no DNA coverage, and be stabilized by simultaneously stacking to the SWNT and hydrogen bonding to neighboring DNAs nucleotides. Also, dopamine can bind to ssDNA-$(GT)_{15}$-SWNT so that it raises neighboring DNA bases. Occasionally, when dopamine stacks on SWNT, DNA nucleotides can also cover dopamine and form stacked sandwich-like structures. The bound dopamine contributes to the potential created at the SWNT surface. Our poses show the electrostatic potential beneath dopamine for several representative binding poses on the SWNT surface. Dopamine binding usually corresponds to extension of the electrostatic potential regions. Such modulations in the potential are likely to affect exciton localization.

**[0072]** Two different mechanisms of binding of dopamine to longer and shorter ssDNA wrapping SWNT are indicated. In the case of ssDNA-$(GT)_{15}$, dopamine is trapped between two ssDNA pitches close to the end of ssDNA-$(GT)_{15}$ where two raised thymine bases trap dopamine However, the mechanism of dopamine adsorption to ssDNA-$(GT)_6$-SWCNT is different; here, dopamine binds between two successive ssDNA-$(GT)_6$'s. The adsorbed dopamine extends the positive and negative potential domains and leads to exciton size extension. Opened water windows by adsorbed dopamine between two ssDNA-$(GT)_6$'s enhances the extension of electrostatic potential pattern leading to less exciton localization at the SWNT surface and brighter PL response of ssDNA-$(GT)_6$-SWCNT conjugates.

**[0073]** Polymer surface density determines density of dopamine binding sites. Our results thus far demonstrate that the conformation of surface-adsorbed ssDNA polymers on SWNT influences SWNT fluorescence and enables tuning of nanosensor responses by affording control over the DNA-SWNT baseline fluorescence. Based on our molecular dynamics and experimental results, we hypothesized that tuning the surface density of $(GT)_6$ on the SWNT surface will affect the resulting SWNT electrostatic footprint, and thus enable more precise control of the baseline fluorescence of the DNA-SWNT conjugate. We therefore varied polymer surface packing by synthesizing DNA-SWNT conjugates with different mass proportions of SWNT (mS) and ss$(GT)_6$-DNA (mD). The resulting DNA-SWNT conjugates thus had variable surface-adsorbed polymer density. We prepared three suspensions at mS/mD mass ratios of 2, 5 and 10. The resulting fluorescence intensity from equimolar SWNT aliquots shows a clear trend whereby higher polymer surface densities (mS/mD=2) exhibit the strongest fluorescence quenching. Addition of 10 μM of dopamine enhances the SWNT fluorescence of all three samples; however, the nanosensor response is highest for the SWNT sample (mS/mD=2) that is most strongly pre-quenched prior to dopamine addition. These results reveal that (i) the degree of fluorescence quenching of SWNT by adsorbed DNA is a function not only of polymer conformation (ring vs. helix) but also of the polymer surface density; the greater the surface coverage, the stronger the SWNT PL quenching; (ii) the higher the surface coverage, the higher the number of dopamine binding pockets; and (iii) dopamine enhances quantum yield in proportion to the number of available binding sites.

## REFERENCES

**[0074]** 1. Manohar, S., T. Tang, and A. Jagota, Structure of homopolymer DNA-CNT hybrids. The Journal of Physical Chemistry C, 2007. 111(48): p. 17835-17845.

**[0075]** 2. Yang, M., V. Koutsos, and M. Zaiser, Interactions between polymers and carbon nanotubes: a molecular dynamics study. The Journal of Physical Chemistry B, 2005. 109(20): p. 10009-10014.

**[0076]** 3. Johnson, R. R., A. T. C. Johnson, and M. L. Klein, Probing the structure of DNA-carbon nanotube hybrids with molecular dynamics Nano Letters, 2008. 8(1): p. 69-75.

**[0077]** 4. Kruss, S., et al., Neurotransmitter detection using corona phase molecular recognition on fluorescent single-walled carbon nanotube sensors. Journal of the American Chemical Society, 2014. 136(2): p. 713-724.

**[0078]** 5. Beyene, A. G., G. S. Demirer, and M. P. Landry, Nanoparticle-Templated Molecular Recognition Platforms for Detection of Biological Analytes. Current protocols in chemical biology, 2016: p. 197-223.

**[0079]** 6. Landry, M. P., et al., Comparative dynamics and sequence dependence of DNA and RNA binding to single walled carbon nanotubes. The Journal of Physical Chemistry C, 2015. 119(18): p. 10048-10058.

**[0080]** 7. Kato, Y., et al., Thermodynamics on soluble carbon nanotubes: how do DNA molecules replace surfactants on carbon nanotubes? Scientific reports, 2012. 2: p. 733.

**[0081]** 8. Schöppler, F., et al., Molar extinction coefficient of single-wall carbon nanotubes. The Journal of Physical Chemistry C, 2011. 115(30): p. 14682-14686.

**[0082]** 9. Choi, J. H. and M. S. Strano, Solvatochromism in single-walled carbon nanotubes. Applied Physics Letters, 2007. 90(22): p. 223114.

**[0083]** 10. Tu, X., et al., DNA sequence motifs for structure-specific recognition and separation of carbon nanotubes. Nature, 2009. 460(7252): p. 250-253.

**[0084]** 11. Johnson, R. R., et al., Free energy landscape of a DNA-carbon nanotube hybrid using replica exchange molecular dynamics Nano letters, 2009. 9(2): p. 537-541.

**[0085]** 12. Salem, D. P., et al., Chirality dependent corona phase molecular recognition of DNA-wrapped carbon nanotubes. Carbon, 2016. 97: p. 147-153.

## 3. An Optical Nanosensor for Imaging Dopamine Neuromodulation in the Extracellular Space of Striatal Tissue

**[0086]** In this example we designed a nanoscale near-infrared fluorescent reporter for neuromodulator dopamine and demonstrate its efficacy for imaging dopamine volume transmission in the extracellular space of both the brain striatum and cortex. The nanosensor images dopamine release and reuptake dynamics in the extracellular space arising from evoked as well as spontaneous release with few-terminal spatial resolution. We show that dopamine volume transmission exhibits highly heterogeneous behavior with apparent dopamine reuptake constants that span over an order of magnitude. Inhibiting dopamine reuptake with antidepressant drug nomifensine reveals that dopamine clearance is predominantly diffusion mediated immediately following release, but dopamine transporter mediated at longer times after release. We observe spatially-correlated dopaminergic signaling dynamics, indicating brain regions of high release synchrony in the striatum. The probe reports dopamine volume transmission at spatial scales that have heretofore been inaccessible with existing investigative tools and can be employed to relate extracellular dopamine concentration dynamics with extrasynaptic receptor activation, neuronal activity, and behavior.

**[0087]** Herein we report a near-infrared fluorescent nanosensor for dopamine (nIRDA) that effectively records dopamine neuromodulation in mouse brain slice preparations. The sensor is synthesized by non-covalently conjugating a $(GT)_6$ polynucleotide sequence to fluorescent single wall carbon nanotubes (SWNT). The sensor provides a reversible up to 3000% ΔF/F fluorescent response upon exposure to dopamine, which is used to image transients in ECS dopamine concentration. The nanosensor provides homogenous labeling of brain tissue, which affords terminal-level spatial resolution, and sensor-analyte binding kinetics that enable video-rate recording of fluorescence modulation with high ##-ms temporal resolution. Our results demonstrate neurochemical imaging of dopamine dynamics in the striatum and cortex ECS with relevance for in vivo investigation of dopamine's critical functions in goal-directed behavior and motor control, and dysfunctions that lead to disease.

**[0088]** Dopamine transients in acute brain slices can be imaged using near-infrared nanosensors

**[0089]** We designed near-infrared fluorescent dopamine sensors (nIRDAs) that report on dopamine in the extracellular space of neuronal tissue. nIRDAs are synthesized from single wall carbon nanotube (SWNT) fluorescent reporters electrostatically conjugated with synthetic polymers to build nanometer-scale probes that can selectively report on local dopamine concentration through a near-infrared change in fluorescence (ΔF/F) of up to 3000% and with a dynamic range of uM to nM dopamine nIRDAs exhibit strongly quenched baseline fluorescence and yield a strong turn-on fluorescent response selectively in the presence of dopamine. Fluorescent nanosensor parameters previously determined as optimal enable nIRDAs to capture low amplitude transients in dopamine concentration arising from the activity of just a few boutons.

**[0090]** We chose to validate nIRDAs by imaging dopamine neuromodulation in acute striatal brain slices. The striatum is a large subcortical structure with homogenous and dense enervation by dopaminergic projections from the SNc. The striatum also receives major glutamatergic afferents from the cortex, whereas medium spiny neurons (MSN), the resident neurons of the striatum are GABAergic. Furthermore, cholinergic interneurons feature prominently in the striatum. nIRDAs exhibit strong selectivity for dopamine over competing neurotransmitter molecules GABA, glutamate, and acetylcholine. We prepared coronal mouse brain slices, which we incubated with 5 $mg.L^{-1}$ of nIRDAs for 10 minutes to enable sensors to localize into the brain tissue. Slices were subsequently rinsed to remove excess or unbound nIRDAs. We found that this method afforded extensive and homogenous labeling of most parts of the coronal slice, including the dorsal striatum, where imaging of dopamine neuromodulation is performed. Furthermore, prior work confirms that SWNT-based fluorophores localize in the ECS of brain tissue.

**[0091]** To image neuromodulation in the striatum with nIRDAs, we evoked dopamine release using both high potassium stimulation (K-stim) and with selective optogenetic stimulation of dopaminergic terminals (L-stim), which ensures that only dopamine is released into synaptic clefts and the ECS. For L-stim, brain slices were prepared from mouse that were virally transfected to express the light sensitive ion channel, channelrhodopsin (Chr2), in dopaminergic terminals of the striatum. Upon optical stimulation with a 473 nm laser, we observe fluorescence modulation of nIRDAs embedded in striatal tissue. The fluorescence modulation is transient whereby its onset coincides with time of stimulation, and is spatially colocalized with dopaminergic boutons exhibiting high degree of Chr2 expression. When slices are labeled with SWNT-polymer constructs that are insensitive to dopamine, no modulation in fluorescence is observed upon repeated stimulation by light. Furthermore, slices that do not express Chr2 in dopaminergic terminals are insensitive to light stimulation as shown by a lack of fluorescence modulation of nIRDAs. Stimulation of wild type striatal tissue slices with high potassium ACSF buffer (15 mM-20 mM $K^+$ ions) also elicits nIRDA fluorescence transients. While light-stimulated dopamine release events in optically active slices are instantaneous and exhibit fast release and re-uptake dynamics (~2 s), stimulation by $K^+$ produces dopamine dynamics that are considerably slower (~10 s). During the course of imaging experiments, we also observe nIRDA fluorescence transients that are not elicited by stimulation but rather occur spontaneously, which we attribute to tonic dopamine release and re-uptake. These results collectively indicate that nIRDAs represent an imaging platform to probe dopamine kinetics in the brain ECS.

**[0092]** Spatial analysis of nIR-DAS fluorescence modulation. A key benefit of imaging neuromodulation lies in the temporally-resolved spatial information that can be garnered from imaging evoked and spontaneous dopamine release. Dopamine concentration transients in the ECS have been studied using electrochemical techniques such as FSCV. Despite the notable role FSCV has played in elucidating DA dynamics in the ECS, it is a tool that assays overflow from the ensemble activity of hundreds of dopaminergic terminals; it is not suited for capturing terminal level spatial information because of the size of the carbon fiber electrode. As a result, information about dopamine volume transmission at interterminal distances has remained largely inaccessible, and the information collected reports on the average behavior of hundreds of terminals, averaging heterogeneities that may be present in individual synapses. nIRDAs provide the spatial granularity required to probe terminal-scale dopaminergic activity to visualize local heterogeneities in dopamine reuptake, the temporal synchrony of release from terminal clusters, and the diffusive evolution of release from a single terminal.

**[0093]** In a representative recording, we analyzed the activity of seven highly active regions of interest (ROI) exhibiting spontaneous (non-evoked) dopamine release and reuptake activity. The regions examined spread over ~100 μm and exhibited synchronized dopamine activity. Correlation analysis revealed the presence of two ROI clusters with high intracluster synchrony and high intercluster asynchrony despite their spread over a 100 μm distance. Our results indicate that neurons can synchronize dopamine release over hundred-micron distances, which is surprising considering that neurotransmitter release is a highly stochastic process with low release probabilities (<10%) for dopaminergic terminals in the striatum. Equally remarkable is the strong asynchrony observed between the two clusters, which indicates the clusters belong to two distinct projection axons with overlapping striatal arborizations. This type of synchronized behavior is observed during imaging of evoked dopamine release as well.

**[0094]** During evoked activity imaging, nIRDA fluorescence modulations can be spatially confined, or can evolve across the imaging field of view, enabling temporal analysis of the spatial evolution of dopamine in the ECS. We present an example of light-stimulated dopamine release for which the spatial granularity afforded by nIRDAs enables tracking of dopamine fluorescence hotspots over a spatio-temporally correlated trajectory. Upon evoked release of dopamine from a terminal or cluster of terminals, a sharp and localized increase in fluorescence and quick clearance thereafter results in the formation of fluorescence hotspots that travel as a function of distance from the release hotspot. This signal attenuates by diffusion and DAT mediated clearance. Analysis of hot spots over their spatial and temporal trajectories reveals the evolution expected from diffusion of molecules from a point of high concentration and their subsequent reuptake as a function of distance. We calculate a propagation of dopamine signal in the ECS exhibiting a quick attenuation in amplitude of ~60% within a 20 μm distance with a temporal delay in the signal of 2 s at a distance of 70 μm from the hot spot.

**[0095]** Kinetic analysis of nIRDAS fluorescence transients. We analyzed kinetics of dopamine modulation from nIRDA fluorescence for evoked (L-stim, K-stim) and non-evoked activity recordings. For each preparation, we analyzed dopamine reuptake rates over multiple slices in the ECS. The dopamine reuptake kinetic parameter, which we report as the ratio of the reuptake rate $r_{max}$ to the Michaelis constant $K_m$ ($k_{uptake}=r_{max}/K_m$), enabled us to compare dopamine reuptake kinetics based on stimulation method. L-stim and non-evoked dynamics yield fastest dopamine reuptake behavior. In comparison, K-stim slices showed an order of magnitude slower dopamine reuptake, likely a consequence of high concentration of $K^+$ ion on the performance of DATs.

**[0096]** We started with an in-vitro sensor calibration curve modified to account for nanosensor saturation by basal dopamine concentrations ex vivo and in vivo. Michaelis-Menten kinetic behavior for dopamine reuptake enables us to extract the parameter $r_{max}$ for select ROIs from the imaging field of view.

**[0097]** Dopamine reuptake inhibitor nomifensine is a common antidepressant drug marketed under Merital or Alival, and slows the clearance of dopamine from the ECS. Nomifensine competitively binds to dopamine transporters, membrane proteins that mediate the reuptake of dopamine, effectively lowering the affinity parameter between dopamine and dopamine transporters. To further investigate dopamine reuptake kinetics, we performed K-stim and L-stim slice experiments in aCSF solution containing 10 μM nomifensine. Following stimulation, we observe an extended persistence in the fluorescence of nIRDAs, consistent with the anticipated slowdown in dopamine clearance from the ECS. Quantitative analysis of dopamine reuptake kinetics shows that application of nomifensine produced significant slowdown in clearance rates for both L-stim and K-stim slices. While the effect of the nomifensine on dopamine clearance is expected, a closer examination of the clearance profile reveals a surprising presence of two distinct regimes. In the first regime, nIRDA fluorescence falls quickly following dopamine release, as expected for DAT-mediated dopamine clearance. The second dopamine clearance regime follows, in which a sudden transition to slower dopamine reuptake is observed. This phenomenon is consistently observed in all striatal brain slices bathed in nomifensine (10 μM). Our results indicate the existence of two dopamine clearance regimes from the ECS. In the first regime, the diffusive flux out of volume is the predominant means by which dopamine concentration decreases. Dominant diffusive clearance occurs immediately following stimulation and release of dopamine The dynamics of this regime is governed predominantly by the effective diffusivity of dopamine in the ECS and the relative proximity of the volume of interest to the release site, and is unaffected by the presence of reuptake inhibiting drugs. In the second regime, DAT-mediated clearance is predominant, in which dopamine reuptake dynamics can be manipulated by drugs that interfere with the DAT-DA affinity parameter.

**[0098]** Analyzing the rise rate of nIRDA fluorescence signals further bolsters our hypothesis of the presence of two dopamine clearance regimes. The dopamine concentration rise rate is a function of proximity to the releasing dopaminergic terminal. Signals obtained from ROIs that are proximal to the dopamine-releasing terminal will show higher rise rates compared to ROIs that are located distal to release sites. Rise rates therefore provide a measure of an ROI's proximity to the releasing terminal. If diffusion mediated clearance is an important component of the computed apparent reuptake constant, $k_{uptake}$, its magnitude will show a positive correlation with proximity to dopamine release sites, and importantly, to the rise rate. This positive correlation is indeed apparent for all evoked and non-evoked data we analyzed. To further substantiate our findings, we implemented a stochastic simulation of dopamine neuromodulation in the dorsal striatum in the presence and absence of nomifensine. Our simulation probes the spatial evolution of a single quantal release of dopamine in the presence ($K_m$=8 μM), and absence ($K_m$=0.2 μM) of nomifensine, and reveals that the clearance of dopamine exhibits dual behavior at distances close to the releasing terminal. The model predicts that close to the releasing terminal the diffusive clearance of dopamine is the dominant process, and thus nomifensine minimally affects the reuptake of dopamine Conversely, in the absence of nomifensine, our model recovers the quick DAT-mediated dopamine reuptake behavior we observe in nomifensine-free slice experiments. Our results illuminate two dopamine reuptake clearance regimes in the presence of a DAT-mediated reuptake inhibitor, regimes likely not observed in data from FSCV measurements in which the spatial profile of dopamine release is averaged over hundreds of termini.

**1**. A functionalized, neurocompatible single-walled carbon nanotube (SWNT) comprising an adsorbed neurotransmitter analyte selective polynucleotide covalently bound to a neurocompatible polyethyleneglycol (PEG).

**2**. The nanotube of claim **1** wherein the polynucleotide is ssDNA or ssRNA

**3**. The nanotube of claim **1** wherein the polynucleotide has a periodic purine-pyrimidine pattern.

**4**. The nanotube of claim **1** wherein the polynucleotide is ssDNA or ssRNA; and

the polynucleotide has a periodic purine-pyrimidine pattern.

**5**. The nanotube of claim **1** wherein the polynucleotide is ssDNA or ssRNA; and

the polynucleotide is polyGT is (GT)n, wherein n is an integer 4-30.

**6**. The nanotube of claim **1** wherein the polynucleotide is ssDNA or ssRNA; and

the polynucleotide is polyGT is (GT)n, wherein n is 6.

**7**. The nanotube of claim **1** wherein the analyte is a neurotransmitter selected from a catecholamine (e.g. epinephrine (adrenaline), norepinephrine (noradrenaline), and dopamine), histamine, 5-hydroxytryptamine (serotonin), γ-aminobutyric acid (GABA), glutamine, glutamic acid or a neurotransmitter metabolite selected from L-3,4-dihydroxyphenylalanine (L-dopa), 3,4-Dihydroxyphenylacetic acid (DOPAC), homovannilic acid and tyramine

**8**. The nanotube of claim **1** wherein the analyte is dopamine.

**9**. The nanotube of claim **1** wherein the PEG is PEG MW 400-20000.

**10**. The nanotube of claim **1** wherein the analyte is dopamine; and

the PEG is PEG MW 400-20000.

**11**. The nanotube of claim **2** wherein the analyte is dopamine; and

the PEG is PEG MW 400-20000.

**12**. The nanotube of claim **3** wherein the analyte is dopamine; and

the PEG is PEG MW 400-20000.

**13**. The nanotube of claim **4** wherein the analyte is dopamine; and

the PEG is PEG MW 400-20000.

**14**. The nanotube of claim **5** wherein the analyte is dopamine; and

the PEG is PEG MW 400-20000.

**15**. The nanotube of claim **6** wherein the analyte is dopamine; and

the PEG is PEG MW 400-20000.

**16**. A functionalized, neurocompatible single-walled carbon nanotube (SWNT) comprising an adsorbed dopamine-selective polynucleotide of sequence $(GT)_6$.

**17**. The nanotube of claim **16** wherein the polynucleotide is covalently bound to a neurocompatible polyethyleneglycol (PEG).

**18**. The nanotube of claiml**6** wherein the PEG is PEG MW 400-20000.

**19**. The nanotube of claim **16** wherein the polynucleotide is covalently bound to a neurocompatible polyethyleneglycol (PEG); and

the PEG is PEG MW 400-20000.

**20**. A method of imaging comprising: detecting changes in extracellular neurotransmitter concentration with the nanotube of claim **1** wherein the changes in extracellular neurotransmitter concentration are detected in neural tissue, and the nanotube is delivered to and/or located in live brain tissue in a brain slice or live mammal.

* * * * *

# Appendix III

# Direct Imaging of Modulatory Neurotransmitters Using Synthetic Nanosensors to Understand and Treat Parkinson's Disease

W81XWH1810282

**PI:** Dr. Jackson T. Del Bonis-O'Donnell **Org:** Regents of the University of California **Award Amount:** $281,112

## Study/Product Aim(s)

- Introduce dopamine nanosensors into acute brain slices of mice and validate use for quantifying stimulated, endogenous dopamine release.
- Quantify differences in dopamine release and reuptake from near-infrared imaging of acute slices from PD model mice.
- Quantify changes in dopamine release and reuptake upon administration of L-DOPA.

## Approach

Our work aims to enable the direct visualization of dopamine transmission in living brain tissue of a PD mouse model leveraging our expertise with a new class of infrared dopamine nanosensors. Detailed measurements of neurotransmission at the molecular level with high spatial and temporal resolution will provide unprecedented insight into the mechanism of dopaminergic aberrations in PD and their effects on neuroplasticity. Additionally, these methods will aid in understanding the interplay of the prescribed drug L-DOPA and changes to dopamine neurotransmission and dyskinesia side-effects.

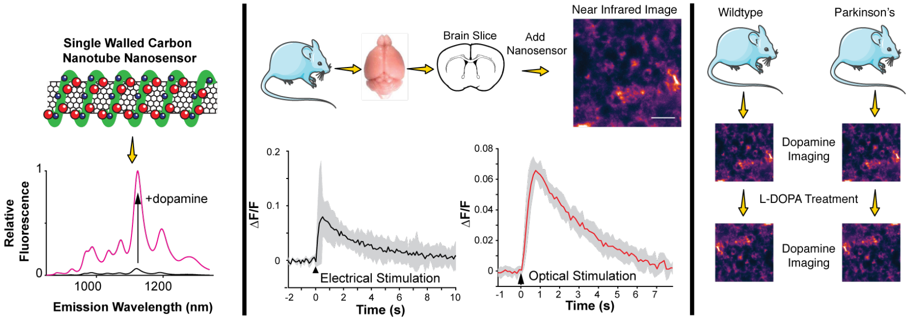

We are using a near-infrared nanosensor for the neuromodulator dopamine to quantify changes in dopamine release and reuptake in Parkinson's mice to determine its role in disease and influence of the therapeutic L-DOPA.

Accomplishment: The quantification of dopamine release was validated using nanosensors in acute slice from mouse brain. Dorsal to ventral gradient in peak evoked dopamine release in striatum was confirmed using this new technology. Confirmed that LPS injections were not inducing Parkinson's phenotype as expected and began troubleshooting. Will repeat experiments in Major Task 2 after resolved.

## Timeline and Cost

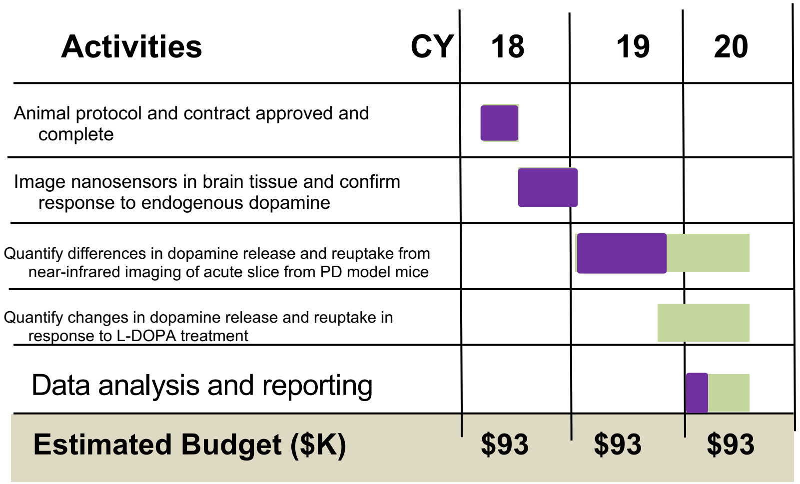

| **Activities** **CY** | **18** | **19** | **20** |
|---|---|---|---|
| Animal protocol and contract approved and complete | 🟪 | | |
| Image nanosensors in brain tissue and confirm response to endogenous dopamine | 🟪 | | |
| Quantify differences in dopamine release and reuptake from near-infrared imaging of acute slice from PD model mice | | 🟪🟩 | 🟩 |
| Quantify changes in dopamine release and reuptake in response to L-DOPA treatment | | 🟩 | 🟩 |
| Data analysis and reporting | | | 🟪🟩 |
| **Estimated Budget ($K)** | **$93** | **$93** | **$93** |

**Updated: 09/17/20**

**Goals/Milestones**

**CY18 Goal** – Animal Protocol Approval, Training and Validation

☑Obtain approval for animal protocol

☑Receive necessary training for animal techniques

☑Validate nanosensor function in brain tissue

**CY19 Goals (NOW CY20 Goals)** – Perform experiments involving PD mice

☑ Perform LPS injections and validate dopaminergic neuron death for PD mouse model (revalidating DA cell death and repeating experiments).

☐ Perform quantitative nanosensor imaging experiments (need to to obtain dataset from newly LPS injected animals).

☑Complete software analysis suite (done) and analyze data (ongoing).

**CY20 Goal** – Perform experiments involving L-DOPA treated mice

☐Perform LPS, SN injections and begin regiment of L-DOPA treatment

☐Perform quantitative nanosensor imaging experiments

☐Prepare manuscript and publish results

**Comments/Challenges/Issues/Concerns**

**Budget Expenditure to Date**

Projected Expenditure: $225k

Actual Expenditure: ~$150k